Geophysical Journal International

*Geophys. J. Int.* (2024) **238,** 902–921
Advance Access publication 2024 June 5
GJI Rock and Mineral Physics, Rheology

https://doi.org/10.1093/gji/ggae195

# Experimental investigation of pore-filling substitution effect on frequency-dependent elastic moduli of Berea sandstone

Y.-X. He [1], S.X. Wang,[1] G.Y. Tang [1], C.H. Dong,[1] C. Sun,[2] S.Y. Yuan[1] and P.D. Shi[3]

[1]*State Key Laboratory of Petroleum Resources and Engineering, College of Carbon Neutral Energy, CNPC Key Laboratory of Geophysical Exploration, Sinopec Oil Reservoir Integrated Geophysical Research Centre, College of Geophysics, China University of Petroleum (Beijing), Beijing* 102249*, China. E-mails: eeyhe*123*@*163*.com (YXH); wangsx@cup.edu.cn (SXW)*

[2]*School of Resources and Geosciences, China University of Mining and Technology, Xuzhou, Jiangsu Province* 221116*, China*

[3]*Swiss Seismological Service, Swiss Federal Institute of Technology Zurich, Zurich CH-*8092*, Switzerland*

Accepted 2024 May 29. Received 2024 May 11; in original form 2024 March 16

## SUMMARY

Based on both forced oscillation and ultrasonic pulse transmission methods, we investigated solid pore infill influences on rock elastic moduli in a broad frequency range $[1 - 3000,\ 10^6]$ Hz for different differential pressures. For a Berea sandstone sample, filled sequentially by solid (22 °C), quasi-solid (26 °C) and liquid (34 °C) octadecane, a frequency-dependence was found for the Poisson's ratio, Young's modulus and bulk modulus, nevertheless, these elastic parameters were strongly suppressed by increasing pressures. Experimental measurements showed that shear wave velocity and modulus of solid-octadecane-filled samples are significantly larger than those of the dry and liquid-octadecane-filled ones, implying the potential stiffening effects related to solid infill in compliant pores. A three porosity structure model, which describes the solid stiffening effects related to equant, compliant and the intermediate pores with aspect ratios larger than those of compliant pores but much less than those of stiff pores, was used to compare against the experimentally measured elastic properties for octadecane pore infill, together with several other fluid/solid substitution theories. The agreement between experimental measurements and theoretical predictions is reasonably good for the sandstone tested, providing that the three porosity model can be applied for pressure- and frequency-dependent elastic moduli estimations for a viscoelastic pore-infill-saturated sandstone. Evaluating the combined squirt flow mechanism responsible for the observed moduli dispersion and attenuation is of great importance to reduce potential errors in seismic AVO inversion and 4-D seismic monitoring of gas-hydrate or bitumen-saturated reservoir, especially for reservoir rocks with complex microstructures and heterogeneous pore types.

**Key words:** Elasticity and anelasticity; Microstructure; Acoustic properties; Seismic attenuation.

## 1 INTRODUCTION

Strengthening our current knowledge of the impacts of changes in pore-filling materials on dynamic elastic properties of porous-cracked rocks might be significant in geophysical practices of seismic exploration and monitoring of heavy-oil, gas-hydrates or bitumen saturated reservoirs (e.g. see Das & Batzle 2008; Han *et al.* 2008; Grechka 2009; Yuan *et al.* 2017; Zhao *et al.* 2017), as well as characterizing $CO_2$ geosequestration, hydrogen storage, contaminant hydrology and nuclear waste storage effects related to salt precipitation and rock frame dissolution (see Vanorio *et al.* 2011). It is thus crucial to reduce uncertainties in these practices through more accurately relating physical properties of reservoir rocks with liquid, solid, or viscoelastic pore infills to their elastic responses. Nevertheless, quantitative rock physics analysis for the integrated influences of rock lithology and the pore infills through direct field measurements is often challenging partially due to limited cores of the investigated specimen volumes. Thus, laboratory experiments (e.g. Batzle *et al.* 2006; Subramaniyan *et al.* 2015; Yin *et al.* 2017, and references therein), theoretical studies (e.g. Deng & Morozov 2016; Han *et al.* 2021; He *et al.* 2022; He *et al.* 2024a, and references therein) and numerical modelling methods focusing on Biot's theory (e.g. Rubino & Holliger 2012; Mallet *et al.* 2017; Quintal *et al.* 2019; Alkhimenkov *et al.* 2020; Caspari *et al.* 2020; Alkhimenkov & Quintal 2022a, 2022b; Zhang *et al.* 2023) are particularly valuable for the non-destructive description of the poro-elasticity of reservoir rocks with viscoelastic pore infills.

The fluid substitution theory of Gassmann (1951), which is independent of pore geometries but relies on porosity, matrix stiffness and fluid, is commonly used to estimate variations in the elastic

moduli for a macroscopically and microscopically isotropic homogeneous bulk rock frame upon fluid property changes. For rocks filled with conventional fluids (e.g. oil and gas), their elastic properties are significantly different from those of rocks filled with highly viscous (e.g. heavy-oil) or viscoelastic solid (e.g. bitumen) infills (e.g. Spencer 2013). In the derivation and application of Gassmann's bulk modulus equation, it is assumed that a rock's pores are interconnected and the fluid pressure remains equilibrated throughout the pore system at sufficiently low frequency. Thus, the Gassmann equations and all their extensions can be invalid at seismic frequencies in the case of pores filled with solid or highly viscous materials or non-Newtonian fluids, as the shear compliance of the pore-filling material with its viscoelastic rheology can strongly restrict pressure communications within the pore space at the representative elementary volume (REV) scale and make Pascal's law inapplicable (e.g. Sun *et al.* 2019a; Solazzi *et al.* 2021). Similarly, the Biot theory, which assumes shear stresses in the pore fluid are insignificant in contrast with those in the solid frame, may not be valid for viscoelastic media in the seismic exploration frequency (e.g. Gurevich *et al.* 2008).

In view of this, several analytical theories were proposed to estimate dynamic elastic moduli of a poroelastic rock filled with highly viscoelastic or solid substances. Gurevich *et al.* (2008) introduced a self-consistent equivalent-medium approach for approximate fluid substitution of heavy-oil, frequency-dependent elastic moduli of which were in general agreement with experimental measurements. They reported the influence of temperature-dependent shear viscosity of the frequency-dependent shear modulus of a saturated rock, and pointed out the underestimated P-wave dispersion can be associated with stiffening effects of squirt flow in heavy-oil-filled samples in the experiments. According to equations in Brown & Korringa (1975), Ciz & Shapiro (2007) proposed a generalized Gassmann approach applicable for calculating an effective elastic tensor of poroelastic media saturated with a highly viscous fluid that behaves as an elastic quasi-solid infill. Their analytical results showed that the effective solid-filled rock shear modulus, which is associated with pore-space volume-averaged strain and relied on pore shape and shear modulus of pore-filling materials, exhibited significant discrepancies from the dry rock shear modulus. Based on the recently presented embedded bound method, Saxena & Mavko (2014) proposed exact substitution equations of modelling solid- or viscoelastic fluids-filled rock stiffness (bulk and shear moduli) using reciprocity from the fluid-saturated and/or dry rock stiffness measurements, for a general case of compression caused heterogeneous mean pressure in pores of arbitrary shape. The substitution equations were expressed in terms of some measureable quantities rather than heuristic pore infill compliance parameters. Moreover, the authors argued that the model in Ciz & Shapiro (2007) may underestimated influences of solid or high-viscosity fluid on rock elastic properties, considering the truth that it did not take into account the spatially non-uniform stresses.

Besides, an increasing number of controlled laboratory experiments confirmed the important role of pore microstructure on rock elastic moduli, which increase with increased differential pressures due to the closure of crack-like soft pores (microcracks; e.g. see Shapiro 2003; de Paula *et al.* 2012; Sun & Gurevich 2020; He *et al.* 2021, and references therein). The soft pores with small aspect ratios were observed usually to possess a more important effect on rock elastic properties compared to those of stiff pores. Also note that most crustal rocks exhibit microcracks with heterogeneous aspect ratio distributions. Although parameters characterizing pore microstructure including the compliant porosity and crack density may not be measured directly, they can be estimated through the pressure dependence of dry rock ultrasonic elastic properties (see David & Zimmerman 2012; Duan *et al.* 2018). On the basics that confining stress causes different pressure gradients in the stiff and compliant porosities, Saxena & Mavko (2015) presented a quantitative model to estimate the influences of solid-saturated soft pores on effective elastic properties. This model shows that the overall rock stiffening are induced by the integrated effects of unrelaxed squirt and shear (viscous solid-squirt) dispersion of rocks filled with solid or high-viscosity infills. However, the model prediction may not be consistent with the low frequency Gassmann theory in the situation of fluid pore infills, as it assumes the soft pores are completely disconnected from stiff pores. Subsequently, a generalized dual-porosity structure for the fluid–solid substitution method was developed in Glubokovskikh *et al.* (2016) to interpret the squirt effects and the partially relaxed condition between the low- and high-frequency limits. The model predictions, nevertheless, show obvious deviations from the experimental measurements, which can be attributed to the oversimplified pore microstructure underlying the model. Indeed, the important difference between the measurements and predictions implies that compliant and stiff pores cannot sufficiently account for the so-called solid-squirt effect in solid substitution experiments, an effect similar to the stiffening influence of local (squirt) fluid flow in fluid-saturated cores, as shown in Makarynska *et al.* (2010) and recognized by Leurer & Dvorkin (2006).

It is also important to realize that, the porous saturated rocks have been long shown to be dispersive, and thus frequency dependence of effective elastic moduli should be taken into considerations when comparing theoretical predictions against laboratory measurements (e.g. see Yin *et al.* 2017; He *et al.* 2022, and references therein). In particular, laboratory experiments have reported that elastic properties of the heavy-oil in its quasi-solid condition possess marked frequency dependence (e.g. see Batzle *et al.* 2006) and correspondingly, the experimental measurements at low frequencies may be strongly different from those obtained at ultrasonic frequencies (e.g. see Han *et al.* 2008; Yuan *et al.* 2016). Therefore, direct laboratory observations of solid stiffening effects on rock elastic moduli in the low seismic frequencies are of considerable importance to help us to understand the squirt mechanisms, as well as how they might affect seismic surveys. However, the related laboratory studies of elastic dispersion and attenuation in solid-filled rocks are very sparsely reported.

During the past two decades, several laboratory apparatus based on the forced oscillation method have been introduced that allow for direct measurements at low frequencies and thus evaluation of the frequency dependence of effective elastic moduli of saturated rocks (e.g. see Batzle *et al.* 2006; Adelinet *et al.* 2010; David *et al.* 2013; Mikhaltsevitch *et al.* 2016; Riviere *et al.* 2016; Pimienta *et al.* 2017; Borgomano *et al.* 2019; Chapman *et al.* 2019; Sun *et al.* 2020, and references therein). Batzle *et al.* (2006) conducted laboratory experiments of low-frequency forced axial oscillations and ultrasonic transmission methods on Uvalde bitumen-saturated carbonate, and discussed the apparent influence of high-viscosity pore infill on frequency dependence of rock elastic properties. Through considering heavy oils in the heavy-oil filled reservoirs as solid materials at room temperature and as liquid infills at higher temperatures, previous experimental studies also showed that shear wave properties in heavy-oil reservoir exhibited stronger temperature dependence at ultrasonic and seismic frequencies than the rock bulk modulus (e.g. see Behura *et al.* 2007; Han *et al.* 2008; Kato *et al.* 2008; Wolf *et al.* 2008). In particular, Spencer (2013) investigated the

effect of temperature and frequency on elastic moduli and the associated attenuation in Ells River bitumen sand at low frequency range (00.2–2.5 Hz), and indicated that the formation heating effect can be sufficiently large to be detected in time-lapse seismic monitoring surveys. More recently, Mikhaltsevitch *et al.* (2019) performed seismic frequency (2 Hz) laboratory measurements on solid (23 °C) and liquid (40 °C) octadecane filled Bentheim sandstone. They found that the stiffening effect of compliant pores on elastic moduli of a rock with solid pore-filling can be negligible at the low frequency and the measured ultrasonic shear modulus is larger than that obtained at the low frequency.

In this work, we conducted a series of laboratory experiments to explore the effects of pore infill on the frequency dependence of the elastic moduli in a Berea sandstone at a range of effective pressures across a wide frequency band, based on the forced oscillation stress–strain approach complemented with the ultrasonic pulse technique. To contribute to current understanding of the combined effects of pore infills and pore shapes (i.e. pores and microcracks), elastic property measurements were performed on the sandstone sample filled sequentially with gas, and solid (22 °C), highly viscous (or quasi-solid) (26 °C) and liquid (34 °C) octadecane. Pressure-dependent moduli dispersion and attenuation upon the sandstone rock saturated with various pore infill phase states were observed and, the potential physical mechanisms responsible for experimental results were investigated. Predictions from several theoretical models were compared against the measured elastic moduli and a fluid–solid substitution model that we derived considering the solid stiffening effects associated with heterogeneous pore types and complex microstructures.

## 2 EXPERIMENTAL METHODOLOGY

### 2.1 Measurement apparatus for dynamic moduli and attenuation

The experimental apparatus, which uses a forced axial oscillation method, for the dynamic Young's modulus $E$ and Poisson's ratio $\nu$ measurements over a wide frequency range of $f = [1 - 3000]$ Hz is illustrated schematically in Fig. 1 (see Yin *et al.* 2017; Sun *et al.* 2020; He *et al.* 2024b). It was designed to be put into a high-pressure container, which can attain confining pressures $P_C$ up to 45 MPa with nitrogen gas and regulate temperature between −20 and 100 °C via heating bath circulation thermostats. The system incorporates a multislice piezoceramic actuator to address a uniaxial sinusoidal force oscillation exerted at top of the testing sample, generating strain amplitudes $< 10^{-6}$. The resulting bulk strain oscillations are recorded using four pairs of BCM semiconductor strain gauges bonded at the core sample centre and another two pairs of strain gauges attached on the bottom end reference aluminium, as shown in Fig. 1(b). From the measured strains, we calculate the complex and frequency-dependent Poisson's ratio $\nu$ and Young's modulus $E$ of a stressed core using (e.g. see Batzel *et al.* 2006):

$$\nu(f) = -\frac{\varepsilon_{\rm rad}(f)}{\varepsilon_{\rm ax}(f)}, \quad E(f) = E_{\rm Al} * \frac{\varepsilon_{\rm Al}(f)}{\varepsilon_{\rm ax}(f)}, \tag{1}$$

where $\varepsilon_{\rm rad}$ and $\varepsilon_{\rm ax}$ represent, respectively, mean radial and axial strains measured from the testing sample, $\varepsilon_{\rm Al}$ is the axial strain of the reference aluminium and $E_{\rm Al}$ is the known Young's modulus for a standard aluminium sample. According to a phase shifts $\theta$ between the stress and strain, tangent of Poisson's phases difference $Q_\upsilon^{-1}$ and extensional attenuation $Q_E^{-1}$ are inferred as (e.g. see Batzel *et al.* 2006; Subramaniyan *et al.* 2015; Sun *et al.* 2020):

$$Q_\upsilon^{-1} = \tan(\theta_{\rm rad} - \theta_{\rm al}), \; Q_E^{-1} = \tan(\theta_{\rm al} - \theta_{\rm ax}), \tag{2}$$

where $\theta_{\rm al}$ and $\theta_{\rm al}$ represent the axial strain phases in the aluminium and the sample, respectively, and $\theta_{\rm rad}$ represents the sample's radial strain phase. Subsequently, the low-frequency bulk and shear moduli, $K$ and $\mu$, of the core sample can be derived using:

$$K = \frac{E}{3(1-2\upsilon)}, \; \mu = \frac{E}{2(1+\upsilon)}, \tag{3}$$

As shown in Fig. 1(b), from the ultrasonic pulse transmission method and the sample's length, we calculate the high-frequency ultrasonic compressional and shear velocities, $V_{\rm P}$ and $V_{\rm S}$, at the frequency of 1 MHz. Combined with bulk density $\rho$, the ultrasonic bulk and shear moduli, $K_{\rm HF}$ and $\mu_{\rm HF}$, can be extracted using:

$$K_{\rm HF} = \rho\left(V_{\rm P}^2 - 4/3V_{\rm S}^2\right), \; G_{\rm HF} = \rho V_{\rm S}^2. \tag{4}$$

Accordingly, ultrasonic Poisson's ratio $\upsilon_{\rm HF}$ and Young's modulus $E_{\rm HF}$ can be inferred as:

$$\upsilon_{\rm HF} = \frac{3K_{\rm HF} - 2G_{\rm HF}}{2(3K_{\rm HF} + G_{\rm HF})}, \; E_{\rm HF} = \frac{9K_{\rm HF} \times G_{\rm HF}}{3K_{\rm HF} + G_{\rm HF}}. \tag{5}$$

In our device, semiconductor strain gauges are bonded onto the sample surfaces with sticky epoxy (Devcon 5 Minute Epoxy) to keep the gauges fixed during the sample sealing and, in particular, to achieve a better coupling between the testing sample and the gauge during dynamic oscillation experiments under influences of different saturation fluid, pressure and temperature, although the actual mechanical coupling is primarily exerted by the confining pressure $P_C$. In addition, for the ease of sample preparation and sealing it with epoxy resin from the nitrogen gas confining medium, a plexiglass-made mould was designed to guarantee that the 12 electric wires connected to the six pairs of strain gauges attached on the sample surface can be fed out. Plenty of experiments proved that this sample sealing technique with the excellent air tightness can both successfully perverse the tested sample and release interface friction between the epoxy and the strain gauges. During all experimental measurements, the pore pressure was successfully regulated steady at approximately 1 MPa using a syringe pump linked to the core sample.

### 2.2 Physical properties of the sandstone sample

The cylindrical rock specimen, measured in this study, is a Berea sandstone precisely grounded to diameter $d = 38.1$ mm and length $L = 71.2$ mm (see Fig. 2). The core plug was drilled, approximately parallel to the poorly determined bedding plane, from an outcrop of Berea sandstone from the western United States. The sample possesses a porosity of ∼20 per cent, and we determined a permeability in the range of $267 \times 10^{-15} - 274 \times 10^{-15}$ m$^2$ (or 267 − 274 mD) by flushing the sandstone core with helium at a gas flow rate of 1.5 ml min$^{-1}$ under controlled differential pressure $P_{\rm diff} = P_{\rm c} - P_{\rm f}$ based on Darcy's law, as shown in Fig. 3. According to X-ray diffraction and polarizing microscope analysis, we obtained the petrophysical properties and mineral compositions of the core plug. The porous sandstone has a quartz content of approximately 80.3 per cent, feldspar 5.3per cent, calcite 3.5per cent and many other fillings such as clays and albite, as listed in Table 1. In accordance with the Voigt–Reuss–Hill average, the elastic properties of rock frame, $K_{\rm g}$ and $G_{\rm g}$, were estimated via volumetric contributions of individual mineral grain and their corresponding elastic properties.

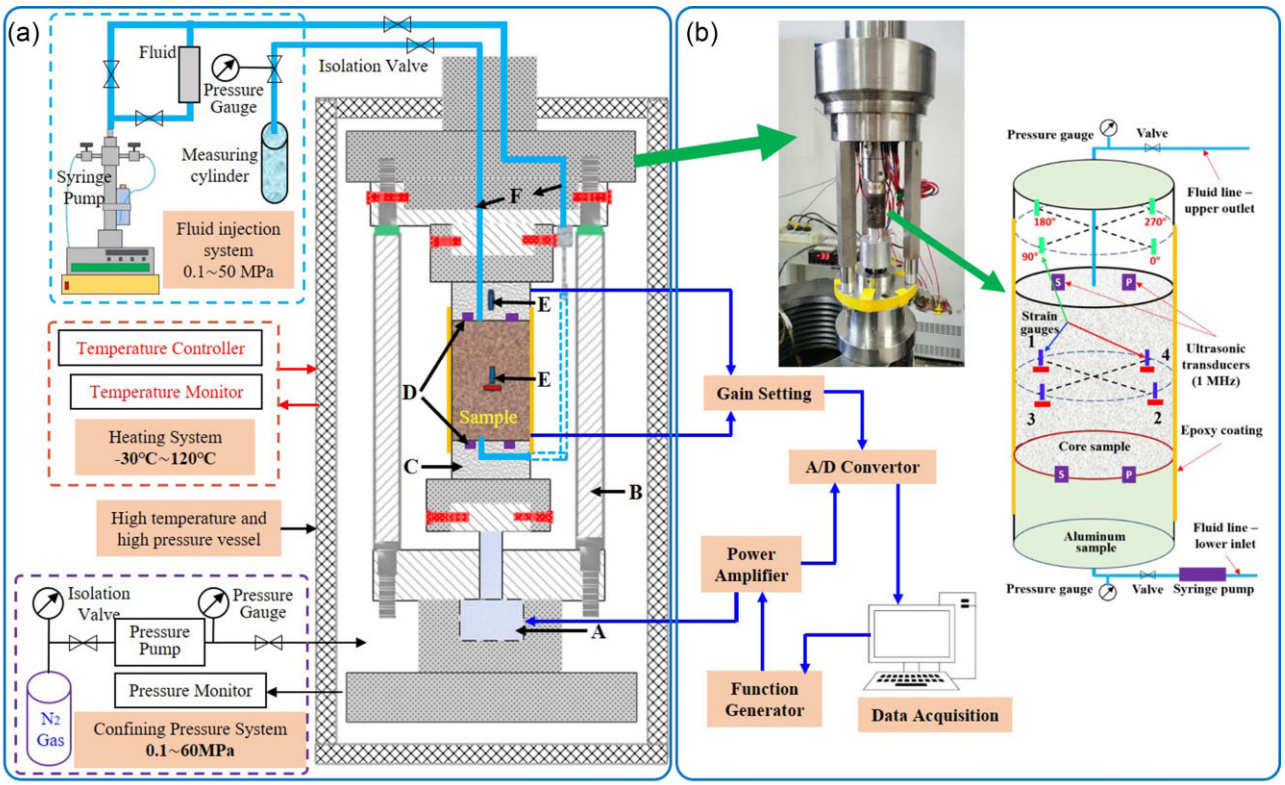


**Figure 1.** Schematic drawings of the multifrequency band elastic parameters measurement apparatus: (a) the low-frequency stress–strain system based on the forced-oscillation method and (b) photograph of the sample stack and the testing core with axial and radial strain gauges. The specific indies represent **A**, oscillator; **B**, support rod; **C**, standard aluminium; **D**, ultrasonic transducers; **E**, strain gauges and **F**, Fluid pipes.

The selected sandstone, consisting of the approximately pure quartz-formed skeleton grains and cement, exhibits complex microstructures of heterogeneous pore types. A core sample of 3.8 mm diameter was imaged with an X-ray microscope (MicroXCT-400) to obtain a comprehensive knowledge of pore microstructure, distribution and connectivity (Figs 2c and d). The assumption of homogeneity and isotropy of a core sample at the REV scale (i.e. volume $\gg$ grain's volume), which represents one key requirement for uniform stress distribution in the low-frequency forced axial oscillation method, is consistently verified through microscopic cross-section images. The different quartz grains of the core specimen exhibits rand grain orientations (Figs 2a and b) and, the average size of mineral grain is around 200 $\mu$m, much smaller than the strain gages length of $\sim$ 5 mm.

### 2.3 Pore-filling substitution procedures

Octadecane $CH_3(CH_2)_{16}CH_3$, which is a hydrocarbon with a melting point at $\sim$ 28 °C, was used as pore infill in its solid (22 °C), quasi-solid (26 °C) and liquid (34 °C) forms in our experimental study. The measured octadecane densities are 778 and 785 kg m$^{-3}$ at pressure of 1 MPa for the liquid and solid phases, respectively, which may cause significant impacts on elastic properties of completely saturated core sample (e.g. Sun *et al*. 2019b; Mikhaltsevitch *et al.* 2019). Accordingly, densities of the core sample, respectively, filled by liquid- and solid-octadecane are close and equal to $\rho_{liq} = 2260$ kg m$^{-3}$ and $\rho_{sol} = 2263$ kg m$^{-3}$. Elastic moduli of $K = 3.82$ GPa and $G = 1.43$ GPa are used for the solid octadecane, and $K = 1.48$ GPa used for the liquid phase, as summarized in Table 2.

Via laying the core sample on the top solid octadecane and heating the target in an oven over 36 hours at temperature $T = 60$ °C, pore system of the core sample can achieve complete octadecane saturation through the vacuum method. After the core plug was evacuated over 48 hr till no bubbles emerged, full fluid saturation can be examined by observing the increased sample weight did not change with time, corresponding to the rock porosity and density of pore-infilling. And vice versa, the pore space can be filled with solid octadecane by cooling the sample down to $T = 22$ °C.

### 2.4 Measurement protocols

During laboratory experiments, the sandstone sample was measured first under dry state with nitrogen gas saturation. Subsequently, the core plug was measured with octadecane-saturated conditions in the solid, quasi-solid (or highly viscous) and liquid forms. Physical properties of the pore-filling materials are listed in Table 2. Prior to experimental measurements of frequency and pressure effects of the dry Young's modulus $E$ and Poisson's ratio $\nu$ at temperature of $T = 22$ °C, the core plug was oven-dried at temperature of $T = 80$ °C during 30 hours to make it consistent with local ambient moisture. Moreover, in order to achieve a balanced stress distribution, exerted pressure was maintained over a period of $\sim$ 2 hr prior to each measurement. It should be mentioned that a constant stress $P = 0.5$ MPa was imposed under axial oscillations to guarantee a great seamless contact between the actuator and the test sandstone. Three low-frequency stress–strain experiments were performed to inspect the repeatability of experimentally measured results at each pressure and, the mean value for all measured data sets was applied

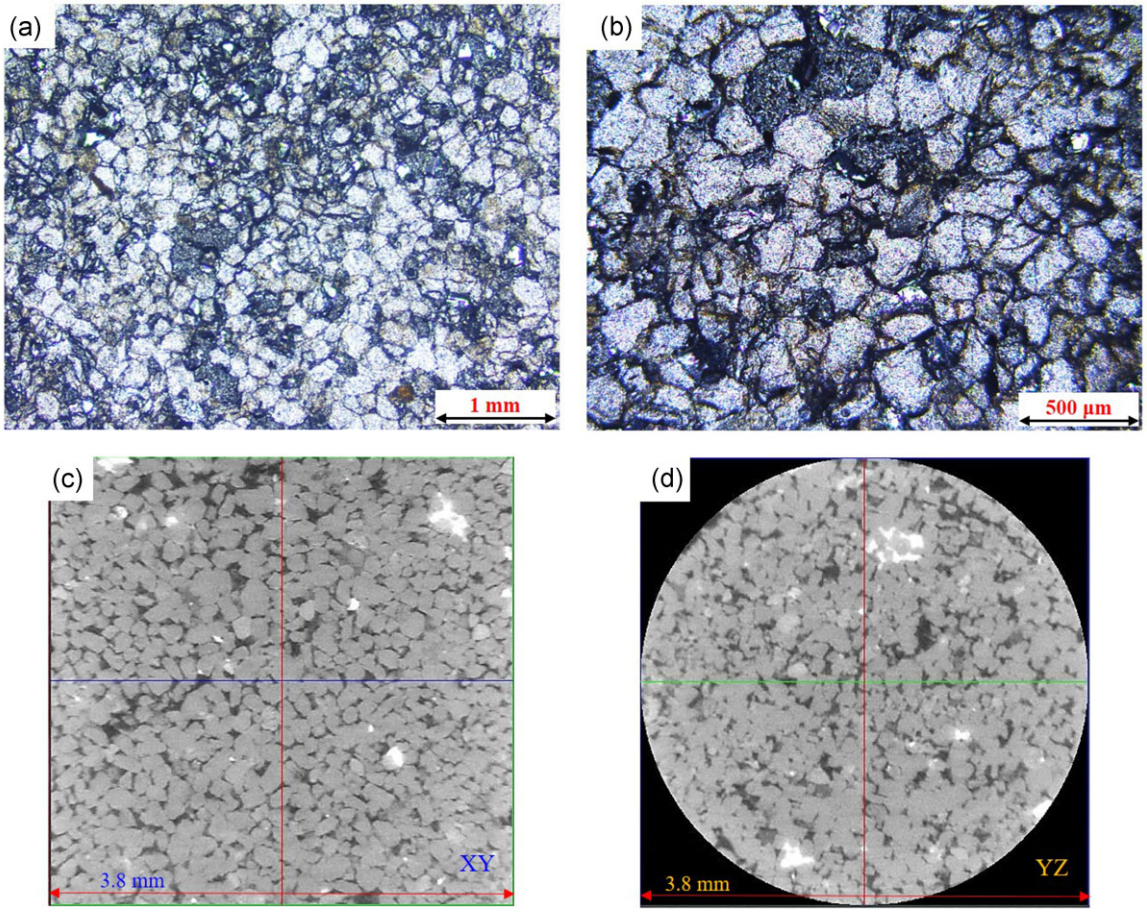


**Figure 2.** Selected 2-D microscopic images illustrating microstructures of the sandstone sample: (a) and (b) thin section photomicrograph at two different scales and, (c) and (d) mutually perpendicular X-ray micro-CT image of core plug with a diameter of 3.8 mm.

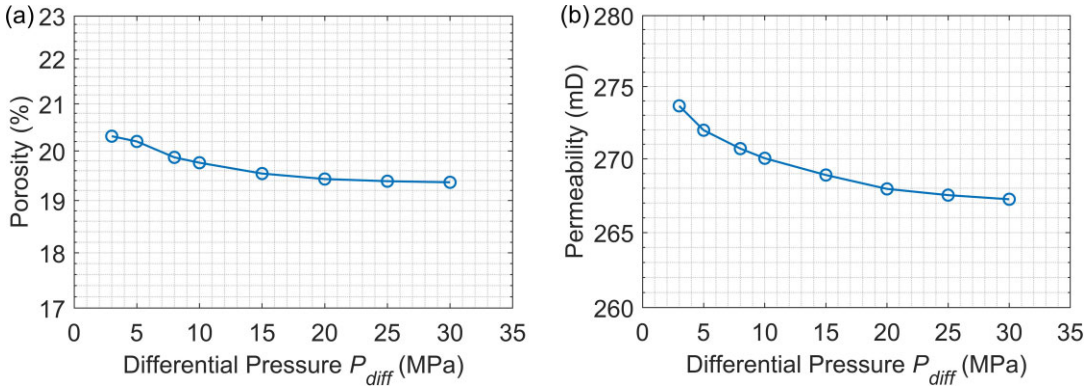


**Figure 3.** Measured (a) rock porosity and (b) permeability variations with differential pressure $P_{\mathrm{diff}}$.

as the final measurement. The system errors in the measured results, as indicated using error bars, may arise from: (i) the bonding of strain gauges and their accuracy limit (gauge factor and resistance deviation), (ii) possible misalignment of the device with the axial stress, (iii) small non-parallelism deviation of core sample preparation and epoxy coatings thickness and (iv) electronic jamming. After the forced axial oscillation measurements, ultrasonic transmission experiments were performed to derive the corresponding high-frequency dry elastic properties.

Following experimental measurements performed for the dry core, the solid-octadecane-filled core was jacked, reassembled into the apparatus. Pressures and frequencies for the forced axial oscillation and ultrasonic transmission experiments were entirely consistent with that for the dry case, but at temperatures of $T = 22$ °C, 26 °C and 34 °C subsequently. Following the measurements of solid-filled sample at $T = 22$ °C, the test vessel was heated at $T = 26$ °C for 12 hr and the core sample was filled with quasi-solid octadecane in the solid form. After that, the sample was heated up to $34 - 36$ °C and the frequency-dependent elastic properties of liquid-octadecane-filled sandstone were measured under the differential pressures used in the previous procedure, but with a constant pore pressure at about $P_{\mathrm{P}} = 1$ MPa.

**Table 1.** Petrophysical properties and mineral compositions of the Berea sandstone used in the experiments.

| Core sample number | Berea sandstone |
|---|---|
| Porosity (at 5 MPa), $\phi$ (per cent) | 20.1 |
| Helium permeability (at 5 MPa), $\kappa$ ($\times 10^{-15}$ $m^2$) | 272.1 |
| Bulk modulus of solid grains, $K_g$ (GPa) | 35.6 |
| Shear modulus of solid grains, $G_g$ (GPa) | 36.2 |
| Density of solid grains, $\rho_g$ (kg m$^{-3}$) | 2638 |
| Length, $L$ (mm) | 71.2 |
| Diameter, $D$ (mm) | 38.1 |
| Dry frame bulk modulus (at 5 MPa), $K_m$ (GPa) | 14.1 |
| Dry frame shear modulus (at 5 MPa), $G_m$ (GPa) | 10.8 |
| Quartz (per cent) | 80.3 |
| Feldspar (per cent) | 5.3 |
| Calcite (per cent) | 3.5 |
| Dolomite (per cent) | 4.3 |
| Clay (per cent) | 3.2 |
| Albite (per cent) | 3.4 |

## 3 EXPERIMENTAL RESULTS

### 3.1 Measurements at seismic frequencies on the dry sample

The frequency dependence of dry Young's modulus $E$ (Fig. 4a) and Poisson's ratio $\nu$ (Fig. 4b), as well as their error bars, measured from the sandstone core filled with nitrogen gas at each differential pressure $P_{\rm diff}$ under axial oscillation are presented in Fig. 4. Their corresponding maximum attenuation $1/Q_{\rm E}$ (Fig. 4c) and $1/Q_{\nu}$ (Fig. 4d) are less than 0.02 and, decrease with the increasing differential pressure. The bulk modulus $K$ (Fig. 4e) and shear modulus $G$ (Fig. 4f) were derived from the measured frequency- and pressure-dependent $E$ and $\upsilon$ using eq. (3). We see that the differential pressure has a significant effect on measured Young's modulus, Poisson's ratio, bulk modulus and shear modulus, which increase by about 100per cent, 38per cent, 111per cent and 65per cent, respectively, with the increase of $P_{\rm diff}$ from 1 to 20 MPa. Within the frequency range of $f = [1 - 3000]$ Hz for the forced axial oscillations, nevertheless, $E$, $\nu$, $K$ and $G$ exhibit negligible frequency dependence (non-dispersive) at each $P_{\rm diff}$, which is likely due to a system response (e.g. Chapman *et al.* 2019; Sun *et al.* 2020; He *et al.* 2022). Attributed to the impact of gradually closing of rock compliant pores, experimentally measured dry $E$ and $\nu$ increase from about 18 GPa and 0.123 at the smallest pressure $P_{\rm diff} = 1$ MPa to about 26 GPa and 0.17 at a relatively higher pressure $P_{\rm diff} = 20$ MPa.

### 3.2 Ultrasonic measurements

For the sandstone sample filled with nitrogen gas (at 22 °C), solid (at 22 °C), quasi-solid (at 26 °C) and liquid (at 34 °C) octadecane (Fig. 5), we observe similar variations of ultrasonic velocities, $V_{\rm P}$ and $V_{\rm S}$, as functions of differential pressure $P_{\rm diff}$. After solid pore substitution to octadecane having a higher bulk modulus, measured $V_{\rm P}$ and $V_{\rm S}$ exhibit the highest velocities (solid green curves in Fig. 5). Correspondingly, the sandstone has a smaller P-wave velocity when filled with nitrogen gas or liquid octadecane of a smaller bulk modulus. At pressures $P_{\rm diff} < 20$ MPa, ultrasonic compressional velocities $V_{\rm P}$ under the dry and liquid filled cases are distinguished by unusually rapid non-linear increase with the increasing pressure $P_{\rm diff}$. As $P_{\rm diff}$ exceeds over 20 MPa, the velocity–pressure curve exhibits approximately linear variations with a decreasing slope. Nevertheless, magnitudes of compressional and shear wave velocities from the dry and the liquid substance filled cores exhibit significant differences. At pressures $P_{\rm diff} > 20$ MPa, on the contrary, $S$-wave velocities $V_{\rm S}$ of the sandstone after fluid substitution to liquid octadecane saturation are lower than those of the dry sample. We observe the obvious 'crossover point' at an intermediate differential pressure of $\sim$ 18 MPa in Fig. 5(b), similar to previous experimental measurements for different kinds of sandstones (e.g. see David *et al.* 2013; Yin *et al.* 2017; He *et al.* 2022).

After heating the sample with solid octadecane (22 °C) pore infills to quasi-solid octadecane (26 °C) saturation, $V_{\rm P}$ decreases by about 60 m s$^{-1}$ while $V_{\rm S}$ decreases by about 300 m s$^{-1}$ at the same differential pressure, which is likely due to the declines of shear modulus of octadecane with the increasing temperature. These results also demonstrate that at $P_{\rm diff} = 30$ MPa when changing the core pore-filling form from the gas-saturated to the fully liquid-octadecane-filled and from the latter to the solid-octadecane-filled, the wave velocities $V_{\rm P}$ increase by $\sim$ 3.8per cent and $\sim$ 14.6per cent, respectively. In addition, shear wave velocity $V_{\rm S}$ in the case of liquid-octadecane saturation at $T = 34$ °C is $\sim$ 11.6per cent smaller than those in the case of solid pore infills at $T = 22$ °C.

### 3.3 Frequency and pressure dependence of the octadecane-saturated sandstone

For the sandstone sample fully filled by octadecane, there are distinctive variation characteristics in elastic moduli dispersion and attenuation under different pressures $P_{\rm diff}$ at different temperatures $T$, as shown in Figs 6–8 at $T = 22$ °C, 26 °C and 34 °C. As measuring frequency increases, Young's modulus $E$ increase at most of differential pressures. Poisson's ratio $\nu$ in the liquid and quasi-solid octadecane-saturated cases tend to increase with the increasing frequency at each pressure $P_{\rm diff}$, while the measured $\nu$ in the solid octadecane-saturated sandstone exhibits fluctuation and appears to slightly decrease. The corresponding attenuation show some frequency dependence phenomenon in Figs 6(c), (d), 7(c), (d), 8(c) and (d). The measured variation of moduli dispersion on the poroelastic specimens can be quantitatively related to the corresponding attenuation using the causality principle typically represented by the Kramers–Kronig (K-K) relationship (e.g. see Mikhaltsevitch *et al.* 2016). The Young's moduli determined from the K-K fitting method with a linear interpolation (solid curves in Figs 6a, 7a and 8a) show a satisfactory fit to experimental measurements over the interested frequencies $f = [1 - 3000]$ Hz. Although the fitting procedure may rely on some particular physical assumptions on the frequency dependence of elastic moduli, the reasonable good agreement between the predicted Young's modulus and the measurements indicates that the measured $E$ and $1/Q_{\rm E}$ are consistent with the Kramers–Kronig relation. This reflects that the measured results are causal and exhibit a common physical source, and hence guaranteeing that our experimental measurements are reliable and related to viscoelastic energy dissipation.

In particular, as frequency increases from 1 to 3000 Hz, the measured Young's modulus $E$ (Fig. 8a) of the completely liquid-octadecane-filled sandstone increases from $\sim$ 19.5 to $\sim$23.5 GPa by 20.5per cent at $P_{\rm diff} = 1$ MPa, the Poisson's ratio $\nu$ (Fig. 8b) from $\sim$ 0.14 to $\sim$ 0.2 by 42.9per cent, the bulk modulus $K$ (Fig. 8e) from $\sim$ 9.2 to $\sim$ 12.6 GPa by 36.9per cent, and the shear modulus $G$ (Fig. 8f) from $\sim$ 8.6 to $\sim$ 9.7 GPa by 12.8per cent. For the quasi-solid and solid octadecane-filled sample, we find that the elastic moduli show similar tendency with those of the liquid-filled case,

**Table 2.** The physical properties of pore-filling materials used in this study.

| Properties of pore-filling materials at 1 MPa | Nitrogen gas (at 22 °C) | Liquid octadecane (at 34 °C) | Quasi-solid octadecane (at 26 °C) | Solid octadecane (at 22 °C) |
|---|---|---|---|---|
| Bulk modulus (GPa) | $K_{\mathrm{NG}} = 0.00142$ | $K_{\mathrm{LO}} = 1.48$ | $K_{SO} = 3.14$ | $K_{\mathrm{SO}} = 3.82$ |
| Shear modulus (GPa) | $G_{\mathrm{NG}} = 0$ | $G_{\mathrm{LO}} = 0$ | $G_{\mathrm{SO}} = 1.12$ | $G_{\mathrm{SO}} = 1.43$ |
| Density (kg m$^{-3}$) | $\rho_{\mathrm{NG}} = 12$ | $\rho_{\mathrm{LO}} = 778$ | $\rho_{\mathrm{SO}} = 782$ | $\rho_{\mathrm{LO}} = 785$ |
| Viscosity ($\times 10^{-3}$ Pa·s) | $\eta_{\mathrm{NG}} = 0.0175$ | $\eta_{\mathrm{LO}} = 3.3$ | $\eta_{\mathrm{SO}} \approx 10^{6}$ | $\eta_{\mathrm{SO}} > 10^{7}$ |

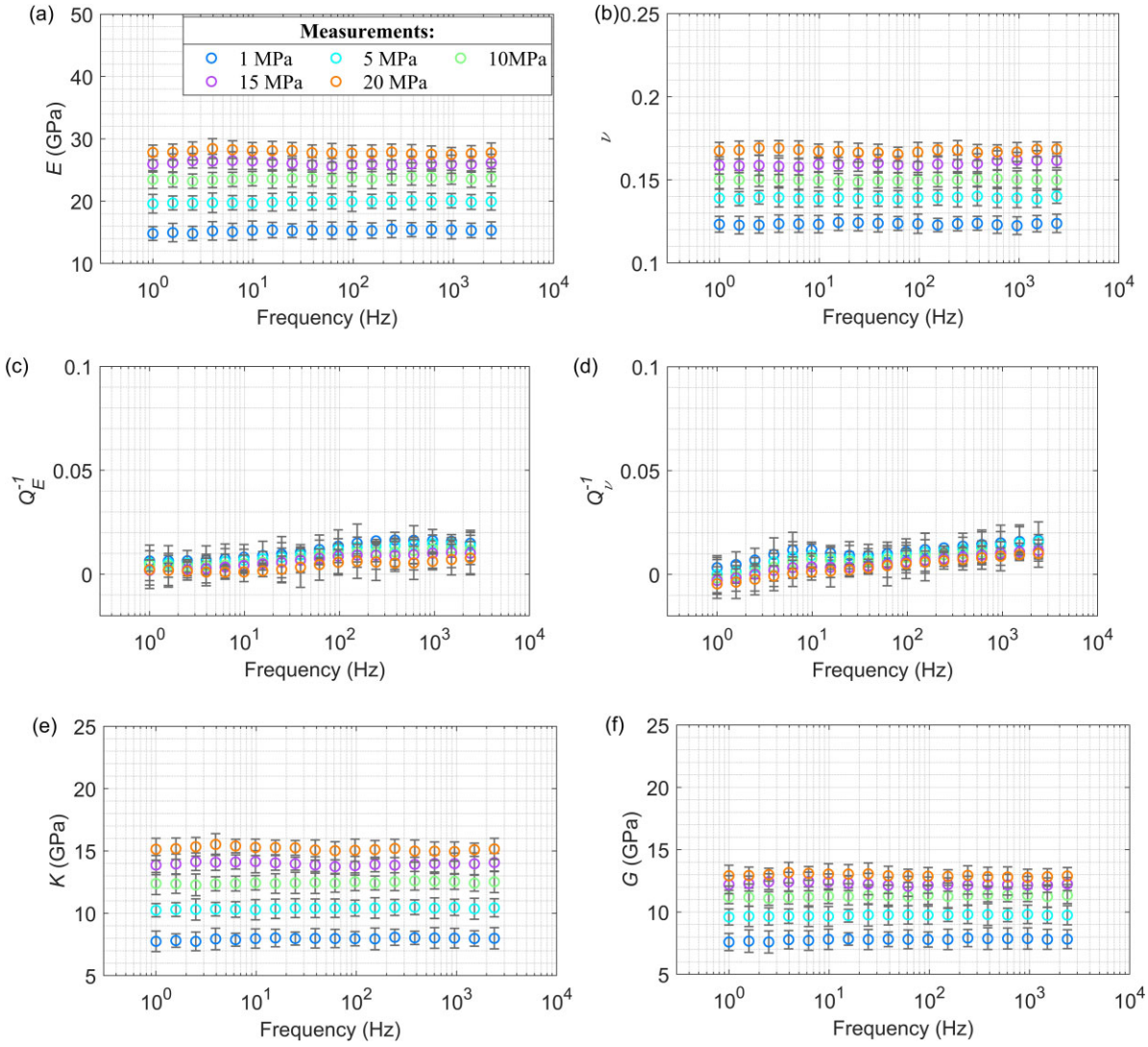


**Figure 4.** The measured frequency dependence of (a) Young's modulus $E$ and (c) its corresponding attenuation $1/Q_E$, (b) Poisson's ratio $\nu$ and (d) its attenuation $1/Q_\nu$, (e) bulk $K$ and (f) shear $G$ moduli for the Berea sandstone filled by nitrogen gas (at 22 °C) at different pressures $P_{\mathrm{diff}}$. Please note that each symbol of open circle represents the mean measurement of three experiments and their corresponding error bars are illustrated.

but with smaller frequency and pressure dependence. The observed discrepancies may be attributed to the difference in the pore infill state at different experimental temperatures, which leads to the increase in bulk and shear moduli and the fluid viscosity due to the variation from liquid to solid octadecane (see Table 2). Furthermore, we observe rapid transitions of $E$, $\nu$, $K$ and $G$, with the change of the core infilling state from the fully liquid-saturated case to the quasi-solid-filled infills and from the quasi-solid-filled case to the solid-filled pore infills. Under any given $P_{\mathrm{diff}}$ at low seismic frequencies, we see $E$ increases by $\sim 5$ and $\sim 7$ GPa, $\nu$ increases by $\sim 0.022$ and $\sim 0.02$, $K$ increases by $\sim 2$ and $\sim 5.5$ GPa, and $G$ increases by $\sim 1.4$ and $\sim 2.8$ GPa, respectively.

In addition, from the low-frequency experimental results, we observe that the largest dispersion and its associated attenuation peaks of measured elastic properties happen at around 165 Hz for liquid-octadecane saturation at 34 °C and at around 1 Hz for the quasi-solid state at 26 °C. It is interesting to find that this frequency dependence and the corresponding attenuation are decreasing with the increasing differential pressure, as well as the increasing viscosity of octadecane as temperature decreases. For pressure $P_{\mathrm{diff}} = 15$ MPa,

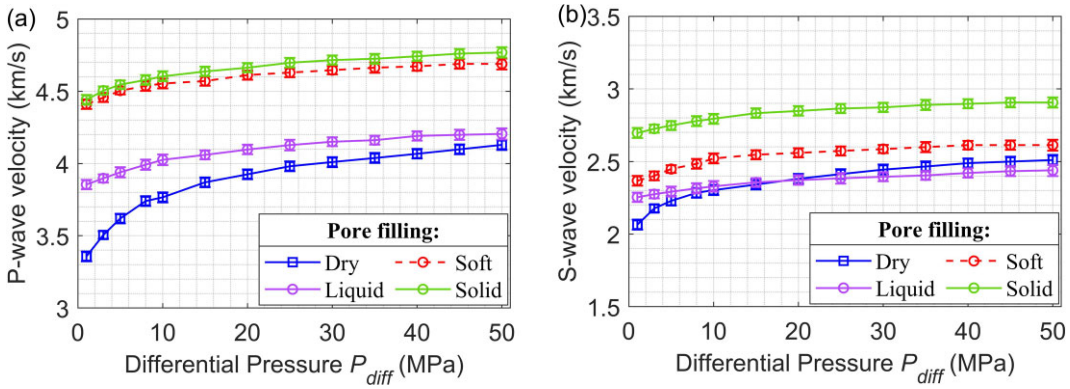


**Figure 5.** Ultrasonic *P*- and *S*-wave velocities experimentally measured on the core sample filled by nitrogen gas (at $T = 22$ °C), solid (at $T = 22$ °C), quasi-solid (at $T = 26$ °C) and liquid (at $T = 34$ °C) octadecane under different differential pressures $P_{\text{diff}}$. Graphs (a) and (b) represent mean values of *P*- and *S*-wave velocities $V_{\text{P}}$ and $V_{\text{S}}$ and their standard error bars.

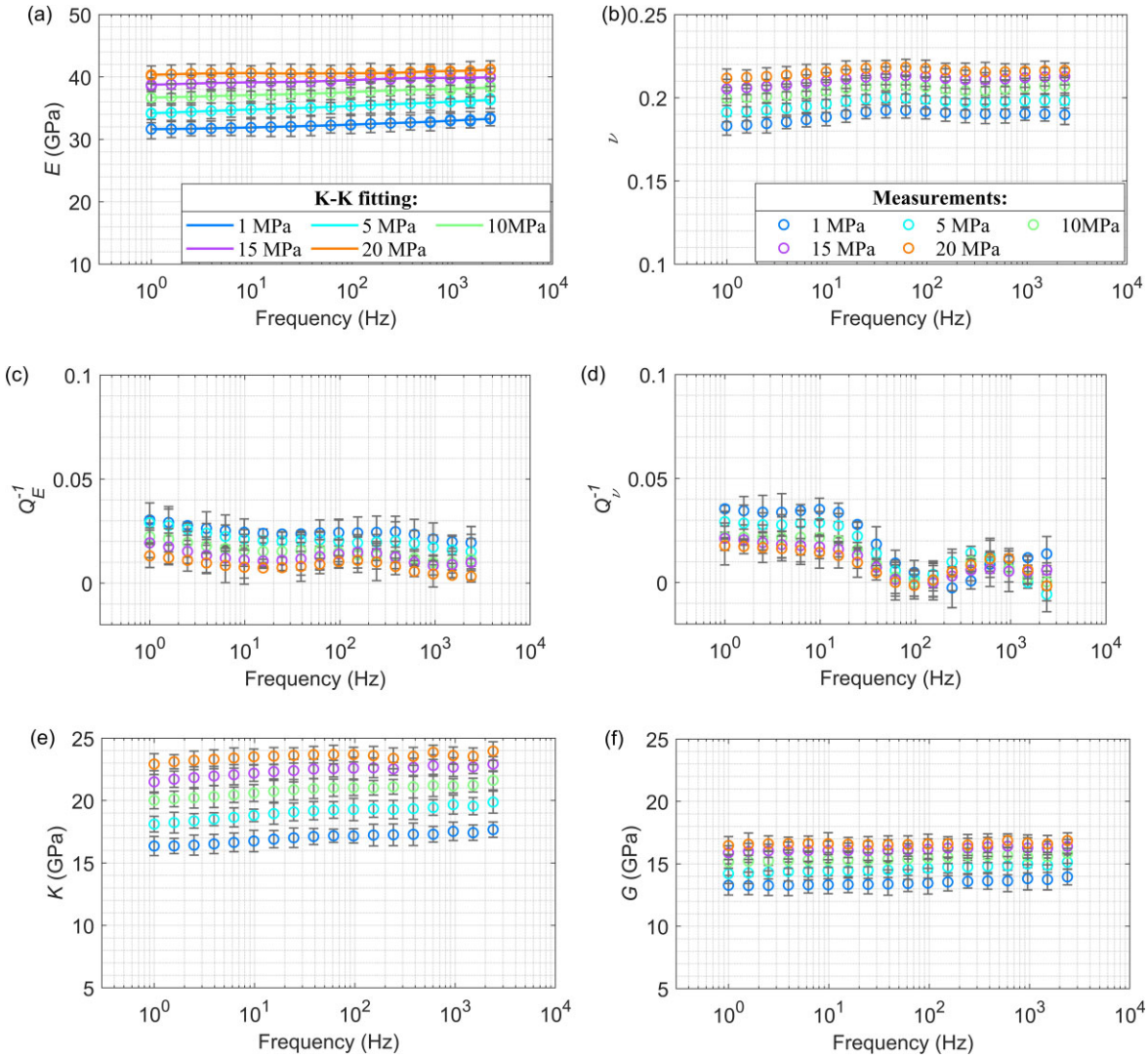


**Figure 6.** The measured frequency dependence of (a) Young's modulus $E$ and (c) its corresponding attenuation $1/Q_E$, (b) Poisson's ratio $\nu$ and (d) its attenuation $1/Q_\nu$ and (e) bulk $K$ and (f) shear $G$ moduli for the sandstone core filled by solid octadecane at $T = 22$ °C under different pressures $P_{\text{diff}}$. In graph (a), solid curves indicate a parametric fit to the laboratory measurements based on the Kramers–Kronig relationship (e.g. see Mikhaltsevitch *et al.* 2016). Note that each symbol of open circle represents the mean measurement of three experiments and their corresponding error bars are illustrated.

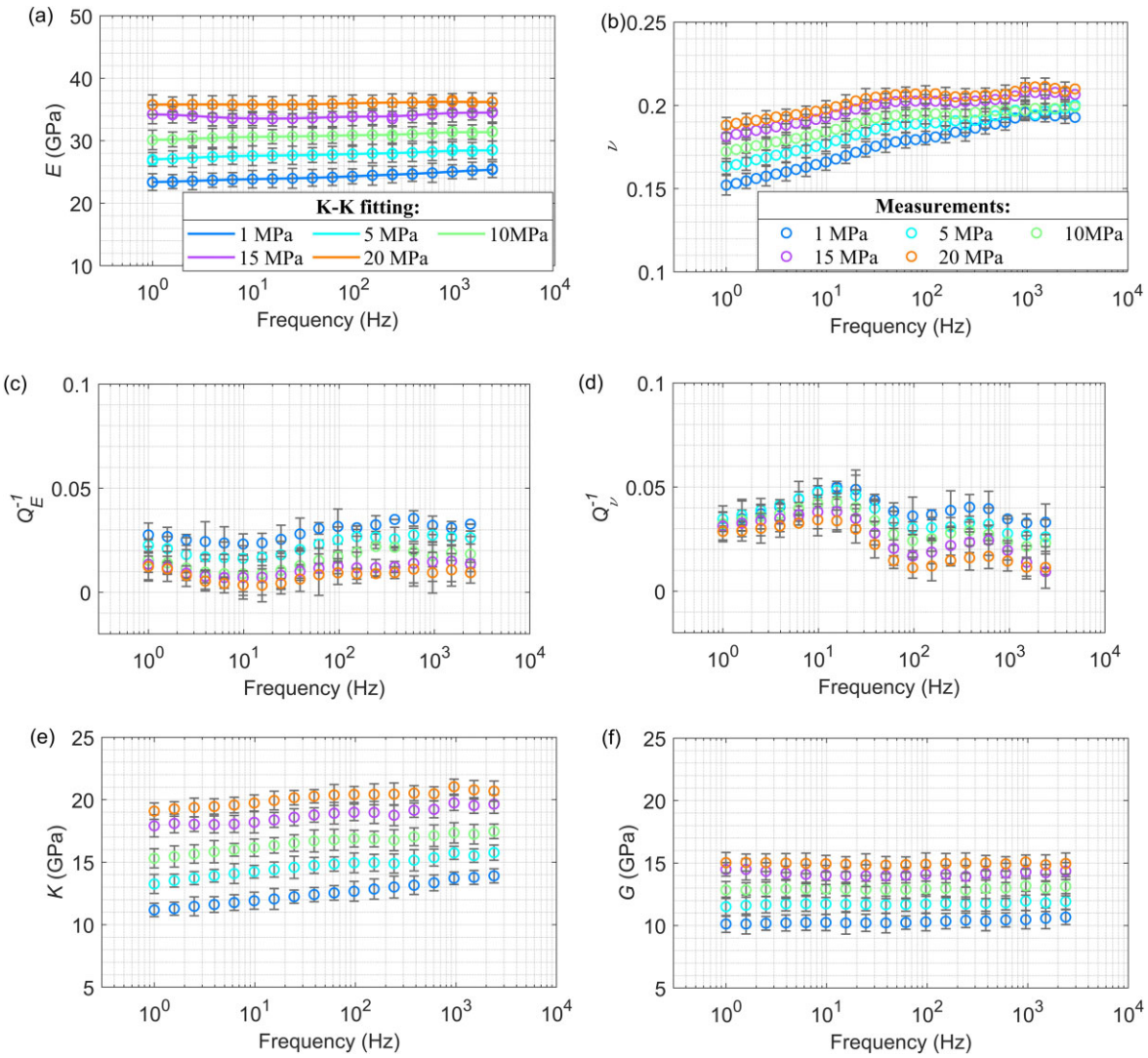


**Figure 7.** The measured frequency dependence of (a) Young's modulus $E$ and (c) its corresponding attenuation $1/Q_E$, (b) Poisson's ratio $\nu$ and (d) its attenuation $1/Q_\nu$ and (e) bulk $K$ and (f) shear $G$ moduli for the sandstone core saturated with quasi-solid octadecane at $T = 26$ °C under different pressures $P_{\text{diff}}$. In graph (a), solid curves indicate a parametric fit to the laboratory measurements based on the Kramers–Kronig relationship (e.g. see Mikhaltsevitch *et al.* 2016). Note that each symbol of open circle represents the mean measurement of three experiments and their corresponding error bars are illustrated.

the measured Young's modulus exhibits nearly no frequency dependence and, apparently the associated attenuation possess peak magnitudes below 0.015 over the seismic frequency band for the case at temperatures of 22 °C and 26 °C. In the case of liquid-octadecane saturation at $T = 34$ °C, nevertheless, the bell-shaped curve of attenuation (Fig. 8c) appears to increase and is consistent with evolution of Young's modulus $E$ at each pressure $P_{\text{diff}}$ (see Fig. 8a).

For a comparison of pore-filling substance and frequency effects, pressure-dependent Young's modulus $E$ and Poisson's ratio $\upsilon$ measured in the sandstone with liquid and solid pore infills at different measuring frequencies $f = [10,\ 100,\ 10^6]$ Hz are illustrated in Fig. 9, together with dry $E$ and $\upsilon$. The values of $E_{\text{HF}}$ and $\nu_{\text{HF}}$ were derived from the measured ultrasonic velocities (see Fig. 4) using eqs (4) and (5). Overall, an obvious distinction between pressure, frequency and pore infills is found. Obtained Young's modulus $E$ and Poisson's ratio $\nu$ exhibit measureable pressure sensitivity under the nitrogen gas and octadecane-filled conditions for frequencies higher than 10 Hz. For measuring pressures of $P_{\text{diff}} = [1,\ 5,\ 10,\ 15,\ 20]$ MPa, $E$ and $\upsilon$ increase with frequency, while the ultrasonic measurements are sharply larger than the low-frequency forced oscillation results. It is easy to understand this experimental observation if we recall that at ultrasonic frequencies, there's no time for rock pore space to equilibrate, resulting in much higher rock stiffness. In particular, for the fully liquid- and solid-filled rock at $P_{\text{diff}} = 5$ MPa, $E$ increases from 24 and 35 GPa to around 30 and 42.2 GPa, and $\upsilon$ increases from 0.155 and 0.197 to around 0.195 and 0.238, respectively. Furthermore, at any given frequency, the liquid-octadecane-filled $E$ and $\upsilon$ measurements are of lower magnitudes as compared with the solid-octadecane-filled results. When the solid infill is substituted with the liquid one, the pressure $P_{\text{diff}}$ seems not to enhance the frequency dependence of $E$ and $\upsilon$. Correspondingly, at any given $P_{\text{diff}}$, phase transition of pore infills causes a decline of deduced ultrasonic results of Young's modulus $E$ by about 42per cent, whereas the Poison's ratio $\nu$ decreases by about 20per cent.

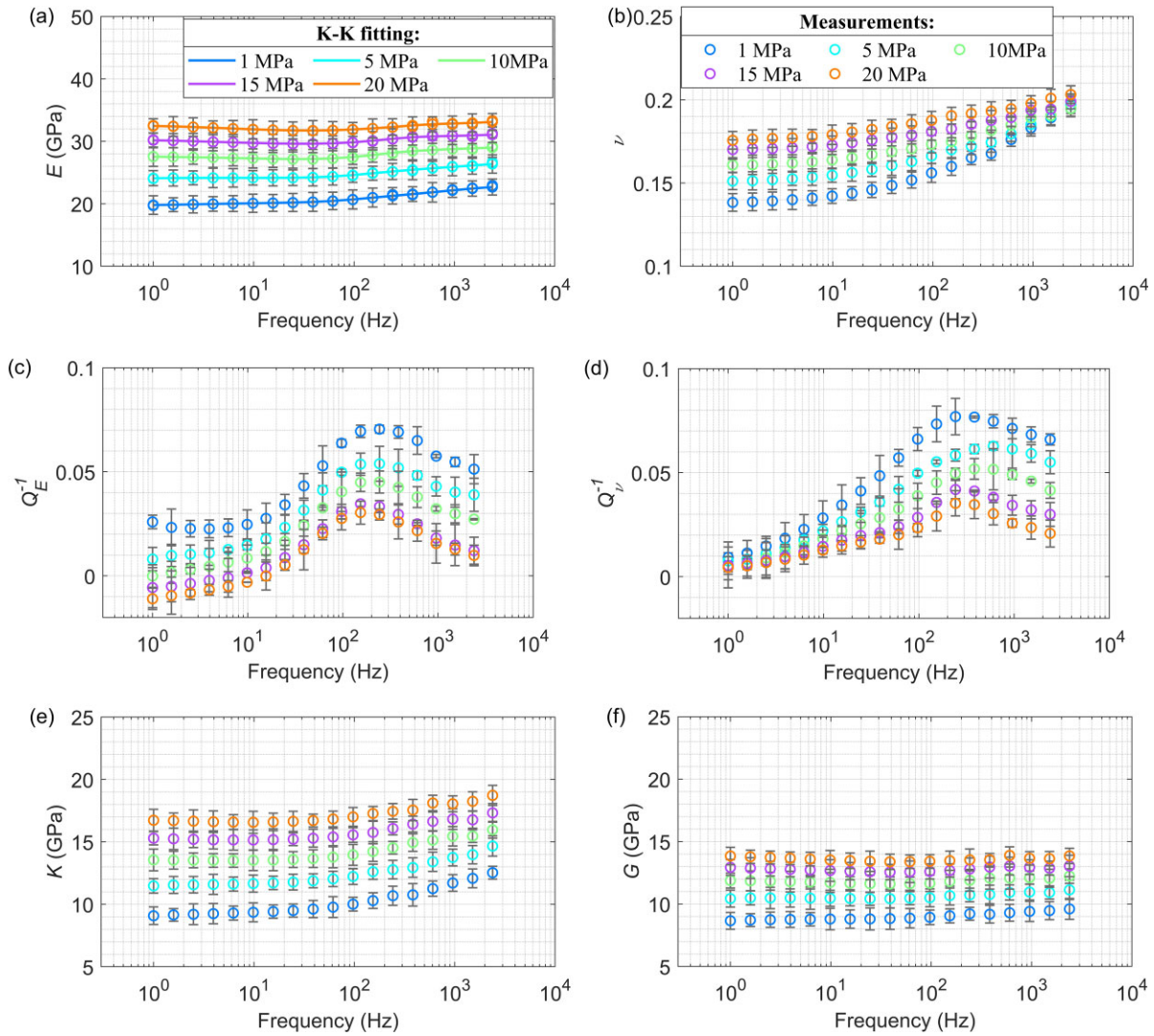


**Figure 8.** The measured frequency dependence of (a) Young's modulus $E$ and (c) its corresponding attenuation $1/Q_E$, (b) Poisson's ratio $\nu$ and (d) its attenuation $1/Q_\nu$ and (e) bulk $K$ and (f) shear $G$ moduli for the sandstone core filled by liquid octadecane at $T = 34$ °C under different pressures $P_{\text{diff}}$. In graph (a), solid curves indicate a parametric fit to the laboratory measurements based on the Kramers–Kronig relationship (e.g. see Mikhaltsevitch *et al.* 2016). Note that each symbol of open circle represents the mean measurement of three experiments and their corresponding error bars are illustrated.

## 4 INTERPRETATION: DISPERSION IN OCTADECANE-SATURATED SANDSTONE OVER THE FREQUENCY RANGE

The non-linear relationship between the steep increase of ultrasonic compressional and shear velocities with differential pressure $P_{\text{diff}}$, especially under relatively low confining pressures (Figs 4a and b), can be likely due to the effect of deforming the pore space and closing cracks having low aspect ratios on the pressure sensitivity of elastic properties of the porous core (e.g. see David & Zimmerman 2012; Duan *et al.* 2018). The increase of pressure $P_{\text{diff}}$ leads to an increase in elastic moduli, related to the strong squeezing of solid grains and gradual closing of thin cracks with various aspect ratios. At sufficiently high $P_{\text{diff}}$ where the compliant pores are substantially closed, nevertheless, dry ultrasonic velocities are approaching to the liquid-filled ones and, discrepancies in rock elastic properties between the seismic and ultrasonic frequencies are gradually reduced (Fig. 9). Apparently, this kind of pressure dependence is rock type dependent and especially depends on pore microstructure parameters (e.g. see de Paula *et al.* 2012; Borgomano *et al.* 2019; Sun *et al.* 2020). In response to pore-filling substitution with octadecane having a higher bulk modulus, the rock stiffnesses also increase, leading to a higher compressional velocity and the derived bulk modulus under the octadecane saturation compared to those in the dry case (Figs 4a and 11a). In addition, considering non-negligible shear compliance of the quasi-solid or solid pore infill, shear wave velocities are significantly higher than the dry and the liquid-saturated ones (Figs 4b and 11b). The discrepancies between shear wave velocities, as well as the deduced shear moduli, under gas and completely liquid-saturated rocks decline gradually with increasing pressure $P_{\text{diff}}$.

### 4.1 Fluid and solid substitution theories

For porous rocks under full saturation, elastic moduli dispersion and attenuation are induced presumably by wave-induced fluid flow (WIFF) at various length scales in pores with different geometries and orientations. Most earlier studies on investigation of aspect ratio

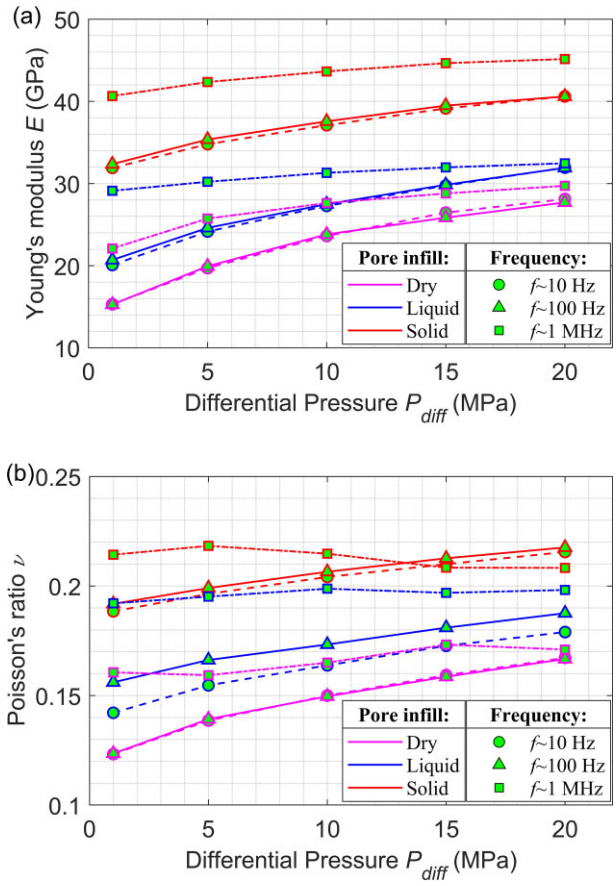


**Figure 9.** Pressure-dependent experimental results of (a) Young's modulus $E$ and (b) Poisson's ratio $\upsilon$ at frequencies $f = [10,\ 100,\ 10^6]$ Hz, respectively, for the Berea sandstone sample saturated with nitrogen gas (magenta line), liquid- (blue line) and solid-octadecane (red line).

distributions of rock microcrcaks are based on the assumption that the pore system of most crustal rocks exhibits a dual-porosity structure including stiff matrix pores ($\phi_s$) and compliant crack-like pores ($\phi_c$) (e.g. see Shapiro 2003; Gurevich *et al.* 2010; David & Zimmerman 2012; Duan *et al.* 2018), or a triple-porosity scheme which is consisted of the equant pore ($\phi_e$) with aspect ratios approximate to 1, moderately stiff (or intermediate) porosity ($\phi_m$) and compliant porosity ($\phi_c$) of often 0.001 or less (e.g. see de Paula *et al.* 2012; Sun *et al*. 2018). By construction, the characteristic aspect ratio of the so-called intermediate pore, in the range of $10^{-3} - 2 \times 10^{-1}$, is much lower than that of the stiff pore but larger than that of the compliant pore. Such moderately stiff porosity may decline exponentially as the pressure increases and close approximately at $P_c = \alpha_s K_e$, where $K_e$ is the bulk modulus of a rock hypothermic rock with only equant pores of usually on the order of the grain bulk modulus and $\alpha_s$ is the fitting pressure sensitivity coefficient. Accordingly, for a sedimentary sandstone, such intermediate porosity is only expected to hypothetically close at confining pressure in the range between 200 and 2000 MPa. Via controlled laboratory experiments, He *et al.* (2022) confirmed that the pressure and frequency dependence of elastic properties in fluid-filled sandstones can be reasonably accounted for using the a generalized model of Triple Pore structure that considers the effects of inhomogeneous Aspect ratio distributions of compliant pores, or referred to as TPA model. For rock porosity described by a mix of three types of pores ($\phi = \phi_e + \phi_m + \phi_c$), the impacts of equant, moderately stiff and compliant pores filled by solid or highly viscous inclusions can be treated sequentially, and two kinds of squirt flow processes exist: squirt between equant and intermediate pores having a high characteristic frequency within normal scope of ultrasonic measurements, and squirt between fractions of stiff ($\phi_s = \phi_e + \phi_m$) and compliant pores occurring at a lower characteristic frequency that may be important in typical seismic frequency range. The frequency and pressure dependence of unrelaxed bulk and shear moduli, $K_{\rm mf}(P, \omega)$ and $G_{\rm mf}(P, \omega)$, for the modified rock matrix associated with the combined squirt flow effects, where $\phi_{\rm m}$ and $\phi_{\rm c}$ are fully saturated with fluid while $\phi_e$ remains empty, can be expressed as (e.g. see Gurevich *et al.* 2010; Sun *et al.* 2019a; Sun *et al.* 2019b)

$$K_{mf}(P,\omega) = \left[\frac{1}{K_{ep}} + \frac{1}{\left(\frac{1}{K_{cp}(P)} - \frac{1}{K_{ep}}\right)^{-1} + \frac{M_{fm}}{\phi_m(P)}} + \frac{1}{\left(\frac{1}{K_{dry}(P)} - \frac{1}{K_{cp}(P)}\right)^{-1} + \frac{M_{fc}}{\phi_c(P)}}\right]^{-1}, \tag{6}$$

$$G_{mf}(P,\omega) = \left[\frac{1}{G_{ep}} - \frac{4}{15}\left[\frac{1}{K_{ep}} - \frac{1}{K_{mf}(P,\omega)}\right] + \frac{1}{G_{fm}} + \frac{1}{G_{fc}}\right]^{-1}, \tag{7}$$

here

$$G_{fm} = \frac{1}{\frac{1}{G_{\rm cp}(P)} - \frac{1}{G_{ep}} - \frac{4}{15}\left(\frac{1}{K_{cp}(P)} - \frac{1}{K_{ep}} + \frac{M_{fm}}{\phi_m(P)}\right)^{-1}} + \frac{5}{2}\frac{G_f}{\phi_m(P)}, \tag{8}$$

$$G_{fc} = \frac{1}{\frac{1}{G_{\rm dry}(P)} - \frac{1}{G_{cp}} - \frac{4}{15}\left(\frac{1}{K_{dry}(P)} - \frac{1}{K_{cp}} + \frac{M_{fc}}{\phi_c(P)}\right)^{-1}} + \frac{5}{2}\frac{G_f}{\phi_c(P)}. \tag{9}$$

In above equations, $\omega = 2\pi f$ denotes angular frequency, $P$ is the differential pressure ($P = P_{\rm diff}$), and $G_f$ represents shear modulus of the pore inclusion. $M_{\rm fm}$ and $M_{\rm fc}$ refer to the effective compressional stiffness of the pore infill for intermediate and compliant pores, respectively. $K_{\rm dry}(P)$ and $G_{\rm dry}(P)$ are rock elastic moduli estimated from ultrasonic dry velocity measurements using eq. (4). $K_{\rm cp}(P)$ and $G_{\rm cp}(P)$ represent the pressure-dependent unrelaxed dry moduli of a hypothetical rock in which all compliant pores are completely closed at relatively high pressures. $K_{\rm ep}$ and $G_{\rm ep}$ denote dry frame elastic moduli of a supposed rock containing equant pores solely and both compliant and intermediate pores are closed completely at the high pressure limit. It is important to mention here that the squirt flow theory in Gurevich *et al.* (2010) assumes the radical fluid flow in rock cracks that is connected to a toroidal pore and therefore, the frequency dependence of this analytical model is not accurate as shown by 3-D numerical solutions of frequency-dependent dispersion and attenuation due to squirt flow in Alkhimenkov *et al.* (2020).

In this work, the effective compressional stiffness of a typical compliant or intermediate inclusion $M_{\rm f}$ can be approximately represented using (e.g. Tsai & Lee 1998; Glubokovskikh *et al.* 2016)

$$M_{\rm f} = K_{\rm f} + \frac{4}{3}G_{\rm f} - \frac{\left(K_{\rm f} - \frac{2}{3}G_{\rm f}\right)^2}{\left(K_{\rm f} + \frac{2}{3}G_{\rm f}\right)\frac{\alpha\gamma_f \cdot I_0(\alpha\gamma_f)}{2I_1(\alpha\gamma_f)} - G_{\rm f}}, \tag{10}$$

where $\alpha$ denotes an inverse aspect ratio of intermediate or compliant pores, $I_k$ denotes the a modified Bessel function of the first kind for the $k$th order, and $\gamma_f = \sqrt{\frac{36G_{\rm f}}{3K_{\rm f}+4G_{\rm f}}}$. According to above formations, when the rock compliant and intermediate pores are fully saturated by an inviscid fluid, $G_{\rm f} = 0$, and hence $M_{\rm fm} = M_{\rm fc} = 0$. Consequently, the partially relaxed rock frame elastic moduli (eqs 6 and 7) can be written as

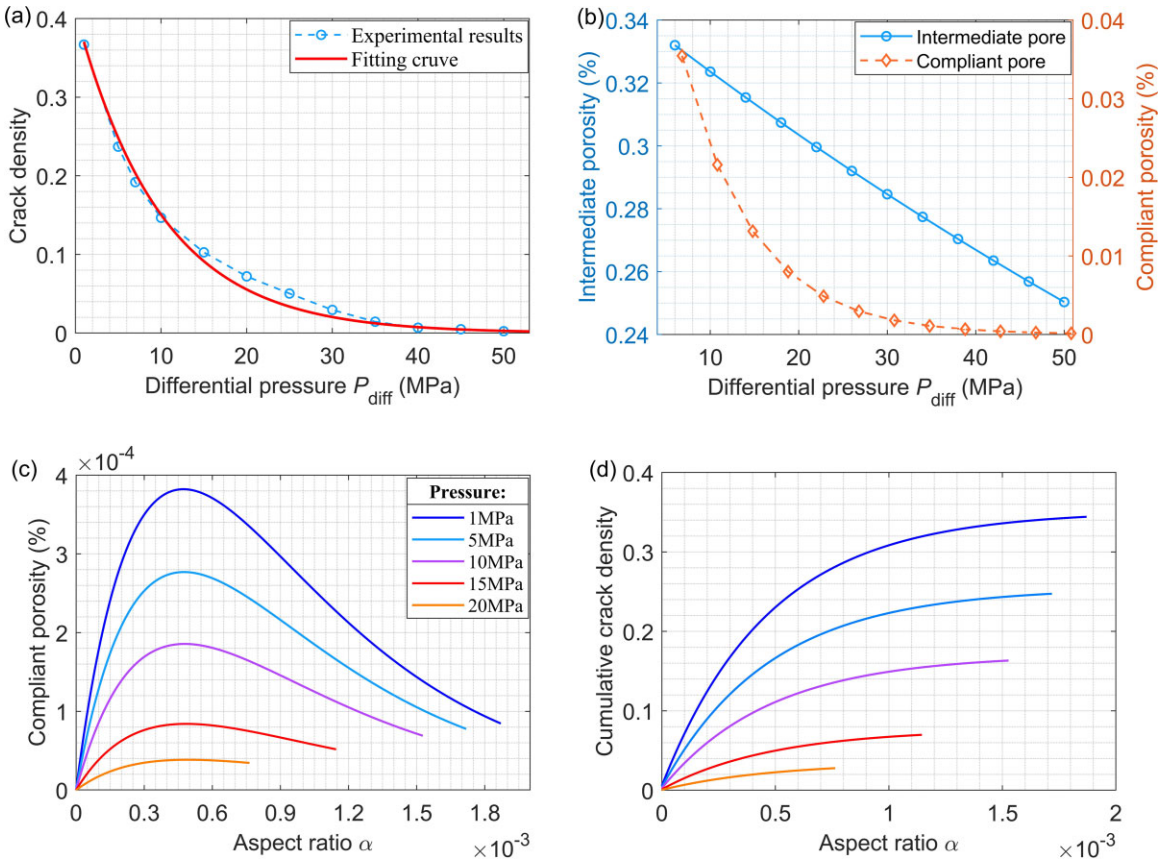


**Figure 10.** (a) The pressure-dependent crack density (blue circle and dashed curve) estimated using the ultrasonically measured dry elastic properties and the fitting curve (solid curve), and (b) the intermediate porosity $\phi_m$ (open circle and blue line) and the compliant porosity $\phi_c$ (open diamond and orange line) at various differential pressure $P_{\rm diff}$. The estimated (c) crack porosity and (d) the cumulative crack density as a function of $\alpha$ at different pressures $P_{\rm diff} = [1,\ 5,\ 10,\ 15,\ 20]$ MPa.

$$K_{\rm mf}(P,\omega) = \left[\frac{1}{K_e} + \frac{1}{\left(\frac{1}{K_{\rm cp}(P)} - \frac{1}{K_{\rm ep}}\right)^{-1} + \frac{3i\omega\eta}{8\phi_m(P)\alpha_m^2}} + \frac{1}{\left(\frac{1}{K_{dry}(P)} - \frac{1}{K_{\rm cp}(P)}\right)^{-1} + \frac{3i\omega\eta}{8\phi_c(P)\alpha_c^2}}\right]^{-1}, \tag{11}$$

$$G_{\rm mf}(P,\omega) = \left[\frac{1}{G_{\rm dry}(P)} - \frac{4}{15}\left[\frac{1}{K_{dry}(P)} - \frac{1}{K_{\rm mf}(P,\omega)}\right]\right]^{-1}, \tag{12}$$

where $\eta$ is fluid viscosity and, $\alpha_m$ and $\alpha_c$ represent aspect ratios of the intermediate porosity $\phi_m$ and compliant porosity $\phi_c$, respectively. Once the unrelaxed elastic moduli, $K_{\rm mf}(P,\omega)$ and $G_{\rm mf}(P,\omega)$, for the modified rock matrix are available, frequency- and pressure-dependent dynamic elastic moduli, $K_{\rm Gass}^{\rm fluid}$ and $G_{\rm Gass}^{\rm fluid}$, of the fully fluid- or inviscid-liquid-saturated rock can be calculated using Gassman's (1951) equation

$$K_{\rm Gass}^{\rm fluid}(P,\omega) = \left[\frac{1}{K_g} + \frac{\phi\left(1/K_f - 1/K_g\right)}{1+\phi\left(1/K_f - 1/K_g\right)/\left(1/K_{mf}(P,\omega) - 1/K_g\right)}\right]^{-1}, \tag{13}$$

$$G_{\rm Gass}^{\rm fluid}(P,\omega) = G_{\rm mf}(P,\omega), \tag{14}$$

where $K_{\rm f}$ and $K_{\rm g}$ denote bulk modulus of the pore infill and the solid mineral, respectively.

Appendix A presents the main procedures for the microstructure estimation of compliant and intermediate pores and, the pressure- and frequency-dependent elastic moduli prediction in fully saturated rocks. The experimentally measured (open circle) and fitted (solid curve) crack density as a function of differential pressure are shown in Fig. 10(a). Fig. 10(b) illustrates the pressure-dependent rock porosities, $\phi_{\rm m}(P)$ (blue) and $\phi_{\rm c}(P)$ (red), of intermediate and compliant pores estimated from the ultrasonic dry moduli measurements, respectively, using $\phi_c^i(P) = \frac{4}{3}\pi\alpha_c^i(P)\Gamma(P)$ and eqs (B5) and (B6). As can be found, the compliant porosity $\phi_{\rm c}$ declines exponentially as the increasing pressure, while the compliant porosity $\phi_{\rm m}$ exhibits a more linear feature at pressures below 50 MPa. The crack porosity $\phi_{\rm c}$ and cumulative crack density $\Gamma$ against compliant aspect ratio $\alpha_c^i$ at five differential pressures are illustrated in Fig. 10(c) and 10(d), respectively. We find the main aspect ratio corresponds to the peak in the curves $\phi_{\rm c}^{\rm i}$ at each pressure $P_{\rm diff}$, and thus the cumulative crack density can be extracted. The obtained total crack density is about 0.34 at $P_{\rm diff} = 1$ MPa, implying that the sandstone specimen represents a typical dual porosity scheme that is controlled by stiff pores and compliant pores with low aspect ratio. This can also be verified from the 2-D microtomographic images in Fig. 2. According to rock microstructural characteristics of compliant and intermediate pores (their porosity and aspect ratio), the TPA model is generalized to consider the effects of complex pore microstructure on dynamic elastic properties.

Alternatively, the undrained frame elastic moduli of a rock with stiff pores fully saturated by solid or highly viscous inclusion can normally be obtained using the isotropic generalized Brown-Korringa's and Gassmann's equations in Ciz & Shapiro (2007; CS

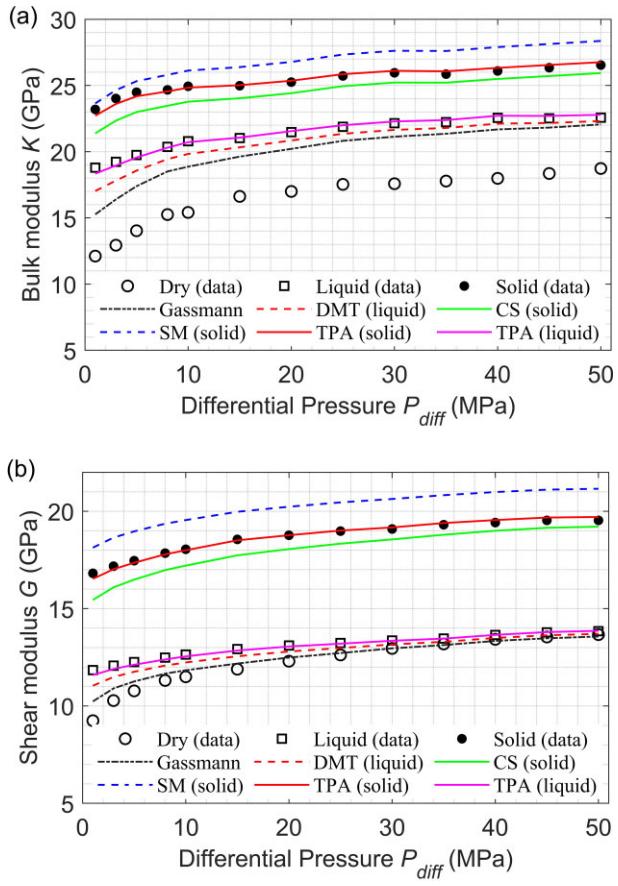


**Figure 11.** Comparisons of the experimental results (black symbols) against theoretical predictions (coloured curves) of (a) bulk modulus $K$ and (b) shear modulus $G$ under different pressures $P_{\text{diff}}$ in the sandstone sample: ultrasonic moduli experimentally measured on nitrogen gas (open circle) and, liquid (open square) and solid (solid circle) octadecane filled core. Elastic moduli, which were predicted using the Gassmann, differential Mori-Tanaka (DMT) and TPA models for the liquid-octadecane-filled cores, as well as using the Ciz-Shapiro (CS), Saxena-Mavko (SM) and the TPA models for the solid-octadecane-filled cores, are illustrated.

model), or through the lower embedded bound method in Saxena & Mavko (2015; SM model) as the induced stress diffusion are likely to be equilibrated in the stiff pore infills. Descriptions of fluid and solid infill substitution based on the CS and SM models in an isotropic homogeneous rock are presented in Appendix B.

In addition, for comparisons with our ultrasonic measurements of the liquid-saturated rock in Fig. 11, a modified Mori-Tanaka model (Mori & Tanaka 1973) and the classical Gassmann (1951) theory in eqs. (13) and (14) were utilized collectively to examine the accuracy and stability of experimentally measured drained rock elastic moduli. In Appendix D, the differential Mori-Tanaka (DMT) model for calculating dry frame moduli is described.

### 4.2 Solid stiffening effect on rock elastic properties

Once all required parameters for fluid/solid substitution relations are derived, experimental results in the liquid- and solid-saturated sandstone were compared against estimations from the theoretical models. In Figs 11(a) and (b), the derived dry elastic moduli (black open circles) from ultrasonically measured velocities exhibit significant pressure sensitivity, which becomes declining strongly for the sandstone with solid pore infills. Estimates of the DMT model (dashed red curves) show a better fit with ultrasonic elastic moduli measurements in the liquid-octadecane-filled sample (black open squares) compared to the predicted results based on the Gassmann theory (dashed black curves), although both theories slightly underestimate the liquid-filled results especially at small differential pressures, which is probably associated with the instability of ultrasonic measurements at relatively small pressures. Compared with the bulk modulus $K$ of a liquid-saturated rock, we see the predicted shear modulus $\mu$ from DMT and Gassmann models show smaller discrepancies to the experimental measurements. However, the differences in predictions are mainly because the ultrasonic laboratory condition based DMT model considers the pore geometry effects, while the low/zero-frequency Gassmann's theory is independent of pore shape variations, indicating elastic moduli dispersion between the low- and high-frequency bands.

The SM model (Saxena & Mavko 2015) significantly overestimates the bulk and shear moduli measurements from the solid-octadecane-filled sandstone, while the CS model (Ciz & Shapiro 2007) produces a more reasonable estimation but still exhibits an observable discrepancy for bulk modulus and shear modulus (Figs 11a and b). After fluid substitution to solid octadecane saturation, $K$ and $\mu$ increase by approximately 1.5 and 1.2 GPa at each differential pressure from the SM model, but both elastic moduli show a decrease by around 0.6 GPa from the CS model. This is probably because the CS model, which follows the assumption of the load-induced homogeneous mean strain and stress distribution throughout the entire pore system, does not introduce stiffening impacts of compliant grain contacts associated with squirt flow between compliant and stiff pores at ultrasonic frequencies related to shear resistance of the solid or highly viscous pore infills. In contrast with model predictions in Sun *et al.* (2019a) based on embedded bound equations, we see that solid substitution through the SM model for the rock having connected or disconnected pores tends to overforecast the measured elastic moduli, as the theory defines the smallest variation upon solid or high-viscosity pore fluid substitution in pore space with compression-induced spatially variant stresses.

The overall rock stiffening effect, which is associated with the squirt and viscoelastic fluid-shear resistance impacts and can be increased dramatically by solid infill, is involved via substituting dry rock elastic properties for unrelaxed frame elastic properties. Such combined influences of squirt flow and solid stiffening on rock elastic properties can be substantial in the presence of solid pore infills, as illustrated with laboratory data examples in the ultrasonic (Fig. 11) and seismic (Fig. 12) frequencies. Moreover, the viscous fluid-shear resistance, which is related to rate-dependent shear tractions due to fluid on the pore boundaries (see Saxena & Mavko 2015), mimics the behaviour of a solid-filled rock at the high-frequency limit and hence, influencing rock elastic properties. This fluid shear mechanism was rarely investigated in geophysics, partially because the shear stresses relax too fast in rocks saturated by low-viscosity fluid. Frequencies at which the squirt flow ($f_{c-sq}$) (Alkhimenkov & Quintal 2022a; Alkhimenkov & Quintal 2022b) and the viscous shear relaxation ($f_{c-sh}$) (e.g. Walsh 1969; Cleary 1978; Mavko 2013; Saxena & Mavko 2015) induced dispersion mechanisms begin to have an impact can be expressed as

$$f_{c-sq} \approx \frac{K_{dry}}{\eta}(\alpha^{sq})^3, \text{ and } f_{c-sh} \approx \frac{G_g}{\eta}\alpha_{c,} \tag{15}$$

where $\alpha^{sq} = h^{sq}/(2l^{sq})$ is the so-called squirt flow aspect ratio that controls the characteristic frequency of squirt flow and, squirt flow thickness $h^{sq}$ describes the crack aperture and $l^{sq}$ represents the 1-D fluid pressure diffusion in the crack. Moreover, the Biot's flow

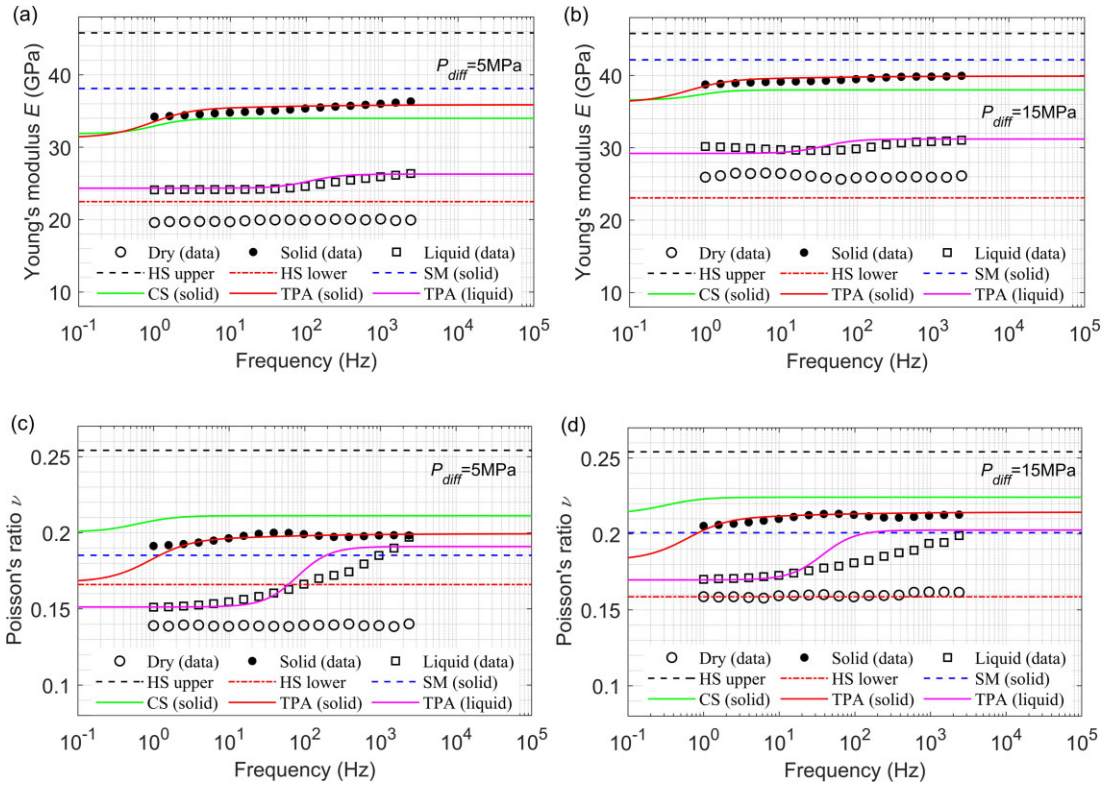


**Figure 12.** Comparisons between the experimental measurements and theoretical predictions for (a and b) Young's modulus $E$ and (c and d) Poisson's ratio $\upsilon$ in the sandstone sample saturated with nitrogen gas (open circle) and, liquid (open square) and solid (solid circle) octadecane, at two differential pressures $P_{\text{diff}} = 5$ and 15 MPa. Please note that octadecane-saturated elastic properties $E$ and $\upsilon$ were predicted using several substitution schemes: HS upper and lower bounds, Saxena-Mavko (SM), the Ciz-Shapiro (CS) and the TPA models. Estimations using the TPA models exhibit a reasonably good agreement with the measured solid/liquid-octadecane-saturated $E$ but a slight discrepancy for the liquid-octadecane-saturated $\upsilon$.

related dispersion might occur at ultrasonic frequencies, and the critical frequency corresponding to the drained/undrained transition is found to be proportional to the rock hydraulic conductivity (i.e. $\kappa/\eta$) such that (Cleary 1978)

$$f_{c-bi} = \frac{4\kappa K_d}{\eta L^2}, \tag{16}$$

where $L$ is the sample's length and $K_d$ is the drained bulk modulus of the tested sandstone sample.

The above analysis implies that the mismatch between the pressure-dependent laboratory measurements and the model predictions of elastic moduli in fluid-saturated rocks might not be sufficiently accounted for with the rock dual porosity structure of stiff and compliant pores, as also stressed in Sun *et al.* (2019b). The TPA theory, which uses heterogeneous aspect ratios of $\phi_m$ and $\phi_c$ (Fig. 10) and may better evaluate the solid stiffening impacts, yields a more precise match with the ultrasonically measured bulk and shear moduli in a core sample with liquid (solid pink curves) and solid pore infill (solid red curves; Fig. 11), respectively. It is also interesting to notice that measured $K_{\text{HF}}$ of the solid-octadecane-filled core exhibits almost no pressure dependence at $P_{\text{diff}} > 30$ MPa, which is generally consistent with the TPA model predictions. Furthermore, $G_{\text{HF}}$ has a slight tendency to grow, in line with predictions from the TPA theory. One possible source for the small discrepancies between the predicted and the measured results lies in the unstable ultrasonic measurements at relatively low pressures, as well as the potentially imprecise estimations of $\phi_m$ and $\phi_c$ and their aspect ratio distributions of the rock with complex microstructure.

Negligible frequency dependence of $E$ and $\nu$ was observed for the Berea sandstone saturated with nitrogen gas at two pressures of $P_{\text{diff}} = 5$ and 15 MPa (Figs 12a–d). The observable varying degrees of moduli dispersion in the liquid-octadecane-filled sample should be related to wave propagation induced fluid movements in rock's porous system. As the viscosity of octadecane increases substantially with fluid–solid substitution, the induced moduli dispersion of $E$ and $\nu$ under the solid-octadecane saturation is almost flat. This phenomenon is likely to correspond to the unrelaxed regime where the pore infill with high viscosity is approximately impossible to flow within the pore spaces, and hence creating a high pressure gradient within each filled-isolated cracks or pores and the suppressed dispersion behaviour. We find the squirt transition frequency, which is scaled as the cube of aspect ratio of compliant pores, of a solid-filled rock is significantly lower compared with the liquid-saturated condition. And thus, it is more appropriate to use a pressure-dependent pore aspect ratio (see Fig. 10), which enables to reflect the rock microstructure property that the increasing pressure caused decline of permeability results in the decrease of fluid mobility.

The measured $E$ and $\nu$ in rocks with solid substances in the pores fall between the HS bounds (Hashin & Shtrikman 1963) (dashed red and dotted black curves), which have a possible range of elastic properties in rocks containing various mineral compositions and solid pore infills (see Tables 1 and 2). The CS approximation (solid green curves) slightly underestimates the laboratory-measured solid-saturated Young's moduli $E$ at low frequencies $f = [1 - 3000]$ Hz, as this CS model assumes equilibrated pore

pressure distribution and its predictions of rock $K_{CS}^{solid}$ ($G_{CS}^{solid}$) in eqs (A1) and (A2) do not involve the $G_f$ ($K_f$) of the pore infill. Moreover, the SM theory (dashed blue curves) significantly overestimates the experimental data, as for the presented ultrasonic bulk and shear moduli in Figs 11(a) and (b). It can be found that Poisson's ratio $\nu$ estimated from the CS model overestimates but the SM model underestimates the experimental results at pressures of $P_{diff} = 5$ and 15 MPa. A comparison between the fluid/solid substitution estimations and the measurements of $E$ and $\nu$ in the fully saturated sample illustrates that the TPA model (pink and red curves) reasonably characterizes the general variations of experimentally measured data as functions of frequency. We believe the reasonably good agreement implies that the combined squirt flow mechanisms between three pore types may have an important role for the moduli dispersion induced by pore-fluid movements. In addition, a comparison of predictions using the presented TPA theory with the several other solid-substitution schemes aforementioned reveals that it is necessary to account for the combined influences of the squirt flow and solid stiffening on the overall elastic stiffness of porous samples filled by solids or high-viscosity fluids. However, we observe some systematic discrepancies of liquid-saturated Poisson's ratio between model predictions and measured data at around the characteristic frequencies of squirt dispersion in Figs 12(c) and (d), which is likely due to the closure of pre-existing microcracks at relatively high pressures.

### 4.3 Variability of frequency effects in Berea sandstone: pore infill and microstructural control

Previous studies pointed out that a variation in bulk and shear moduli of rocks filled with solid or highly viscous materials may arise from mechanical changes of rock framework and pore structure induced by differential pressure (e.g. see Christensen & Wang 1985; Ciz & Shapiro 2007; Gurevich *et al.* 2008). The differences estimated in octadecane-filled effective elastic moduli at the measured frequencies of $f = [10, 10^6]$ Hz are displayed in Fig. 13. At the lowest pressure $P_{diff}$, the porous sandstone exhibit the largest sensitivity of moduli variation to the pore infill phase state transition, except for the bulk modulus $\Delta K$ measured at $f = 10$ Hz which has weak pressure dependence for all saturation conditions (Fig. 13a). These non-linear relationships between elastic moduli changes and differential pressure may be attributed to the gradual closing of compliant pores with little aspect ratios as wave velocities variation against pressure. As pressure $P_{diff}$ increases, rock solid grains are compacted tightly, accompanied by closure of compliant pores and the decline of rock surface areas in contact with the inclusions. The resulted increase in surface energy associated with the fluid-solid interaction may eventually lead to a reduction in rock moduli variations (see Yin *et al.* 2019). Additionally, we see bulk moduli $K$ in the liquid-, quasi-solid- and solid-octadecane-saturated cases are increased by 27.8per cent, 55.6per cent and 113.2per cent with respective to the dry rock condition under the lowest pressure at the low frequency $f = 10$ Hz, and by 54.6per cent, 91.7per cent and 119.8per cent at the high ultrasonic frequency $f = 1$ MHz. Meanwhile, the shear moduli $G$ increase by 25.6per cent, 44.9per cent and 84.6per cent at frequency $f = 10$ Hz and, by 27.2per cent, 40.8per cent and 82.6per cent at frequency $f = 1$ MHz.

To the authors' knowledge, only the measured results of low-frequency experiments for solid substitution in sandstone samples by Mikhaltsevitch *et al.* (2019) presented such an obvious stiffening effect of bulk and shear moduli. Even though the frequency dependence of rock elastic moduli may in some conditions dissimulate the real moduli stiffening at high ultrasonic frequency, the solid-saturated elastic moduli measured at low frequencies here were not significantly affected by the rock stiffening effect associated with dispersive characteristics. Furthermore, variations in shear stiffening of the solid-octadecane-saturated rock versus increasing differential pressure are more obvious than those of the bulk stiffening measured in the low-frequency band. Correspondingly, bulk stiffening variations with $P_{diff}$ are much more apparent than the shear stiffening at the ultrasonic frequency. It has been accepted that pore pressure has no time to equilibrate among pores or cracks of varying compliances at high frequencies, while the pressure may partially equilibrate at seismic frequencies and rock elastic moduli may rely not only on differential pressure but also on frequency and rock microstructure. It is thus reasonable to observe much larger variations in saturated bulk moduli ($\Delta K$) measured in the ultrasonic frequency at each pressure $P_{diff}$ compared to those obtained in typical seismic frequencies.

## 5 CONCLUSIONS

Laboratory experiments exploring dispersion of elastic properties were performed in a broad frequency range of $f = [1 - 3000, 10^6]$ Hz on a sample of sandstone with pore infills ranging from gases to solids state at differential pressures ranging from 1 to 20 MPa. The porous sample was filled sequentially by gas, liquid or solid pore-filling material that was assumed to be much smaller in elastic properties compared to constituent materials, to imitate the rock fluid–solid substitution patterns. Laboratory experiments yielded comprehensive data set for elastic properties and the associated attenuation as functions of frequency for each considered phase state of octadecane pore infill at different pressure $P_{diff}$. Elastic properties of the gas-filled sample exhibit negligible frequency dependence, while the corresponding moduli in the octadecane-saturated rock show observable dispersion and attenuation effect. The general trend of the frequency dependence indicates the effects of squirt flow related to pore infills. For pore infill in its quasi-solid and solid states, the frequency dependence of elastic properties was observably smaller compared with that in the liquid-filled rock and was largely reduced with the increasing differential pressure. This variation in elastic properties is partially because a rock saturated with high-viscosity pore infills is much more difficult to compress than that one under the dry condition and hence, suppressing its pressure and frequency sensitivities in the existence of compressible microcracks. Another observation illustrates that shear wave moduli and velocities of the solid-octadecane-saturated rock are significantly larger compared to those of the dry or the liquid-octadecane-saturated case, which strongly points to the stiffening effect of solid infill that is very likely pronounced in the presence of huge compliant pores with heterogeneous aspect ratio distributions. Moreover, as temperature decreases, the characteristic frequencies of these frequency-dependent saturated elastic moduli tend to shift to lower values with the increase of octadecane viscosity. These experimental measurements were in reasonable accordance with the potential impact for micromechanisms of pressure-induced porosity closing, which results in limited volume of viscous fluid flow among pores of various aspect ratios and the rock permeability is thus largely reduced due to poorer connectivity of the pore structure.

We introduced a squirt flow model that takes into account the influence of pore microstructure to compute elastic moduli dispersion

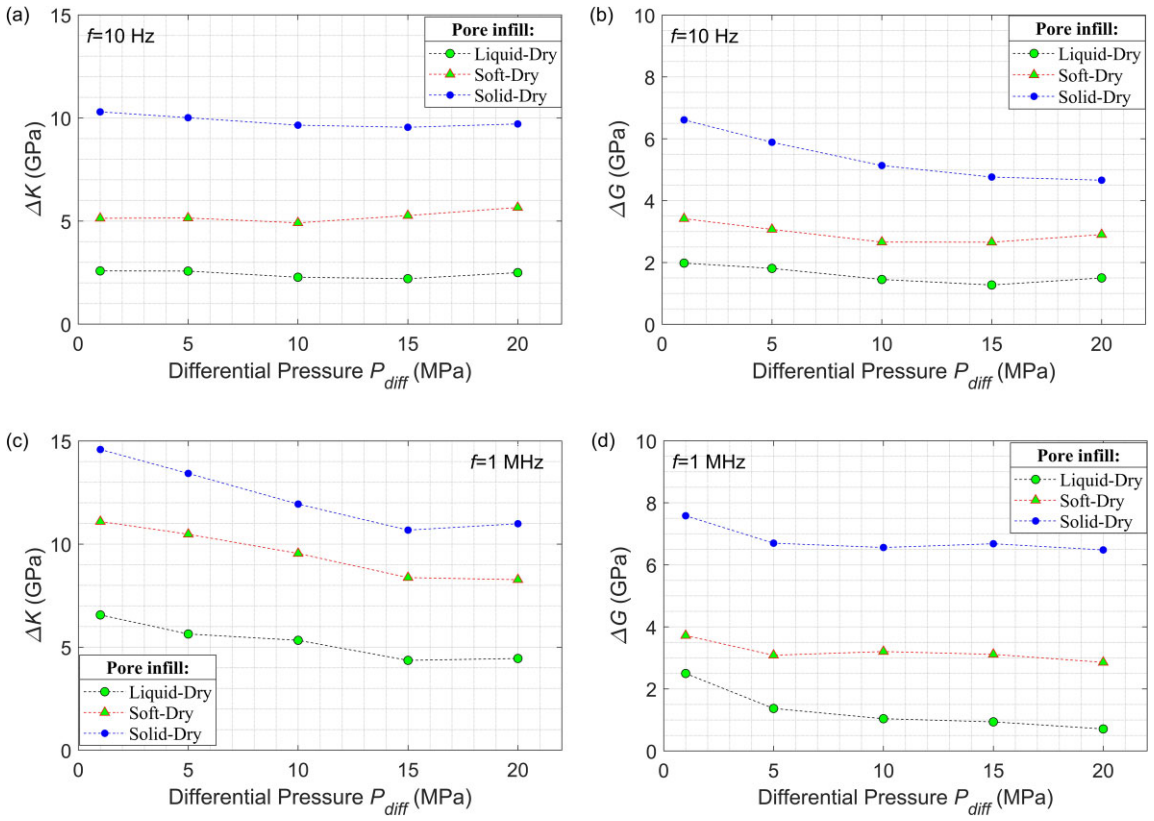


**Figure 13.** The differences between the dry and octadecane-filled bulk and shear moduli at two different frequencies of (a and b) $f = 10$ Hz and (c and d) $f = 1$ MHz as functions of pressure $P_{\text{diff}}$ for the Berea sandstone.

and attenuation in a porous rock with solid or highly viscous pore infill. Geometrical parameters characterizing the pore space in the analytical model can be derived in the laboratory using pressure dependence of ultrasonically measured dry velocities. Our laboratory-measured results from the Berea sandstone saturated by octadecane in seismic and ultrasonic frequencies were compared against predictions of the present TPA model at different pressures, along with several other fluid and solid substitution schemes that cannot be used to appropriately characterize the solid pore infill influences related to the stiffening of the compliant grains' contact. The CS model largely underestimates the solid-octadecane–saturated elastic moduli of $K$, $G$ and $E$ due to neglecting the stiffening effects related to squirt flow between stiff and compliant pores, while the SM model significantly overestimates the measurements as it assumes the compliant pores are isolated from the stiff pores and the stress in the pore infill is not uniform. It is important to note that the assumption of the rock embodying three types of pores is a crude simplification in regard to the realistic pore geometries. Nevertheless, our experimental measurements and theoretical predictions of such treatment are in a reasonably good agreement for the solid-filled Berea sandstone, in which the induced stresses are spatially uniform in the pore system.

Although our presented method involves extracting pore structure parameters via fitting of the measured dry ultrasonic moduli, this model strengthens our ability to characterize several key differences of stiffening effects in pressure and frequency dependence of elastic moduli due to solid infills in the compliant pores, compared to previous analytical models. This phenomenon indicates that the squirt dispersion mechanisms of equant, intermediate and compliant pores have a significant impact on compression and shear stiffness of the solid-octadecane–saturated core sample and hence, successfully quantifying the combined effects of squirt mechanism on rock elasticities may have its potential applications in further seismic inversion and time-lapse seismic monitoring of heavy-oil, gas-hydrates or bitumen-saturated reservoir properties. However, it seems very interesting that the predicted characteristic frequencies of Young's modulus and Poisson's ratio for the solid-octadecane–saturated specimen appear at values lower than the measured frequency range. In addition, the presented model is suitable for pure sandstone as the pressure impacts on the dry elastic properties are dominantly controlled by the closure of compliant pores. Thus, confirmation of this observation and prediction requires further laboratory measurements of seismic dispersion and attenuation for a broad range of lithological rocks of complex pore microstructures at a wide frequency band.thin the range of critical porosi

## ACKNOWLEDGMENTS

Authors sincerely thank the two editors and the two anonymous reviewers for their very constructive comments and suggestions that help us greatly to improve the quality of this paper. The work presented is financially supported by the National Natural Science Foundation of China (41930425, 42374129), the Beijing Natural Science Foundation (8222073), the R&D Department of China National Petroleum Corporation (Investigations on fundamental experiments and advanced theoretical methods in geophysical prospecting applications, 2022DQ0604-01) and National Key R&D Program of China (2018YFA0702504).

## AUTHOR CONTRIBUTIONS

Y.-X. He (Conceptualization [Lead]), Methodology [Lead], Writing-original draft [Lead]), S.X. Wang (Investigation [Lead], Funding acquisition [Lead]), G.Y. Tang (Formal analysis [Lead], Writing-review & editing [Equal]), C.H. Dong (Visulalization [Equal], Writing-review and editing [Equal]; C. Sun (Validation [Equal], Resources [Equal]), S.Y. Yuan (Formal analysis [Equal], Methodology [Equal]), and P.D. Shi (Writing-review & editing [Equal], Invetigation [Equal])

## DATA AVAILABILITY

All experimental data and models presented in this study can be reproduced and are available at https://github.com/EEYHE123/Solid-pore-infill.git.

## REFERENCES


Adelinet, M., Fortin, J., Guéguen, Y., Schubnel, A. & Geoffroy, L., 2010. Frequency and fluid effect on elastic properties of basalt: experimental investigations, *Geophys. Res. Lett.,* **37**(2), doi:10.1029/2009GL041660.

Alkhimenkov, Y. & Quintal, B., 2022a. An accurate analytical model for squirt flow in anisotropic porous rocks—Part 1: classical geometry, *Geophysics,* **87**(2), MR85–MR103.

Alkhimenkov, Y. & Quintal, B., 2022b. An accurate analytical model for squirt flow in anisotropic porous rocks—Part 2: complex geometry, *Geophysics,* **87**(6), MR291–MR302.

Alkhimenkov, Y., Caspari, E., Gurevich, B., Barbosa, N.D., Glubokovskikh, S., Hunziker, J. & Quintal, B., 2020. Frequency-dependent attenuation and dispersion caused by squirt flow: three-dimensional numerical study, *Geophysics,* **85,** MR129–MR145.

Batzle, M.L., Han, D.H. & Hofmann, R., 2006. Fluid mobility and frequency-dependent seismic velocity—direct measurement, *Geophysics,* **71**(1), N1–N9.

Behura, J., Batzle, M., Hofmann, R. & Dorgan, J., 2007. Heavy oils: their shear story, *Geophysics,* **72**(5), E175–E183.

Berryman, J.G., 1995. *Mixture Theories for Rock Properties Rock Physics & Phase Relations: A Handbook of Physical Constants,* pp. 205–228, ed. Ahrens, T.J., America Geophysical Union.

Borgomano, J., Pimienta, L., Fortin, J. & Gueguen, Y., 2019. Seismic dispersion and attenuation in fluid-saturated carbonate rocks: effects of microstructure and pressure, *J. geophys. Res.,* **124,** 2019JB018434.

Brown, R.J.S. & Korringa, J, 1975. On the dependence of the elastic properties of a porous rock on the compressibility of the pore fluid. *Geophysics,* **40,** 608–616

Caspari, E., Greenwood, A., Baron, L., Egli, D., Toschini, E., Hu, K. & Holliger, K., 2020. Characteristics of a fracture network surrounding a hydrothermally altered shear zone from geophysical borehole logs, *Solid Earth,* **11**(3), 829–854.

Chapman, S., Borgomano, J., Yin, H.J., Fortin, J. & Quintal, B., 2019. Forced oscillation measurements of seismic wave attenuation and stiffness moduli dispersion in glycerine-saturated Berea sandstone, *Geophys. Prospect.,* **67**(4), 956–968.

Christensen, N.I. & Wang, H.F., 1985. The influence of pore structure and confining pressure on dynamic elastic properties of Berea sandstone, *Geophysics,* **50**(2), 207–213.

Ciz, R. & Shapiro, S., 2007. Generation of Gassmann equations for porous media saturated with a solid material, *Geophysics,* **72**(6), A75–A79.

Cleary, M.P., 1978. Elastic and dynamic response regimes of fluid-impregnated solids with diverse microstructure, *Int. J. Solids Struct.,* **14,** 795–819.

Das, A. & Batzle, M., 2008. Modeling studies of heavy oil—in between solid and fluid properties, *Leading Edge,* **27**(9), 1116–1123.

David, E.C. & Zimmerman, R.W., 2012. Pore structure model for elastic wave velocities in fluid-saturated sandstones, *J. geophys. Res.,* **117**(B7), doi:10.1029/2012JB009195.

David, E.C., Fortin, J., Schubnel, A., Gueguen, Y. & Zimmerman, R.W., 2013. Laboratory measurements of low- and high-frequency elastic moduli in Fontainebleau sandstone, *Geophysics,* **78**(5), D369–D379.

de Paula, O.B., Pervukhina, M., Makarynska, D. & Gurevich, B., 2012. Modeling squirt dispersion and attenuation in fluid-saturated rocks using pressure dependency of dry ultrasonic velocities, *Geophysics,* **77**(3), WA157–WA168.

Deng, W.B. & Morozov, I.B., 2016. Solid viscosity of fluid-saturated porous rock with squirt flows at seismic frequencies,. *Geophysics,* **81**(4), D395–D404.

Duan, C.S., Deng, J.X., Li, Y., Lu, Y.J., Tang, Z.Y. & Wang, X.B., 2018. Effect of pore structure on the dispersion and attenuation of fluid-saturated tight sandstone. *J. Geophys. Eng.,* **15**(2), 449–460.

Gassmann, F., 1951. Über die elastizität poröser medien, *Vierteljahrsschrift der Naturforschenden Gesellschaft in Zürich,* **96,** 1–23.

Glubokovskikh, S., Gurevich, B. & Saxena, N., 2016. A dual-porosity scheme for fluid/solid substitution, *Geophys. Prospect.,* **64**(4), 1112–1121.

Grechka, V., 2009. Fluid-solid substation in rocks with disconnected and partially connected porosity, *Geophysics,* **74**(5), WB89–WB95.

Gurevich, B., Makarynska, D., de Paula, O.B. & Pervukhina, M., 2010. A simple model for squirt-flow dispersion and attenuation in fluid-saturated granular rocks, *Geophysics,* **75**(6), N109–N120.

Gurevich, B., Osypov, K., Ciz, R. & Makarynska, D., 2008. Modelling elastic wave velocities and attenuation in rocks saturated with heavy oil, *Geophysics,* **73**(4), E115–E122.

Han, D.H., Liu, J. & Batzle, M., 2008. Seismic properties of heavy oils—Measured data, *Leading Edge,* **27,** 1108–1115.

Han, X., Wang, S.X., Tang, G.Y., Dong, C.H., He, Y.X., Liu, T., Zhao, L.M. & Sun, C., 2021. Coupled effects of pressure and frequency on velocities of tight sandstones saturated with fluids: measurements and rock physics modelling, *Geophys. J. Int.,* **226**(2), 1308–1321.

Hashin, Z. & Shtrikman, S., 1963. A variational approach to the elastic behaviour of multiphase material, *J. Mech. Phys. Solids,* **11,** 127–140.

He, Y.-X. *et al.* 2024a. Laboratory experiments and theoretical study of pressure and fluid influences on acoustic response in tight rocks with pore microstructure, *Geophys. Prospect.,* **21**(1), 162–181.

He, Y.-X. *et al.* 2024b. A seismic elastic moduli for the measurements of low-frequency wave dispersion and attenuation of fluid-saturated rocks under different pressures, *Pet. Sci.,* **21,** 162–181.

He, Y.-X., Wang, S.X., Sun, C., Tang, G.Y. & Zhu, W., 2021. Analysis of the frequency dependence characteristics of wave attenuation and velocity dispersion using a poroelastic model with mesoscopic and microscopic heterogeneities, *Geophys. Prospect.,* **69**(6), 1260–1281.

He, Y.-X., Wang, S.X., Xi, B., Tang, G.Y., Yin, H.J., Zhao, L.M., Sun, C. & Ma, X.Y., 2022. Role of pressure and pore microstructure on seismic attenuation and dispersion of fluid-saturated rocks: laboratory experiments and theoretical modelling, *Geophys. J. Int.,* **23**(3), 1917–1937.

Kato, A., Onozuka, S. & Nakayama, T., 2008. Elastic property changes in a bitumen reservoir during steam injection, *Leading Edge,* **27,** 1124–1131.

Krief, M., Garat, J., Stellingwerff, J. & Ventre, J., 1990. A petrophysical interpretation using the velocities of P and S waves (full-waveform sonic), *Log Analyst,* **31,** 355–369.

Kuster, G.T. & Toksöz, M.N., 1974. Velocity and attenuation of seismic waves in two-phase media, *Geophysics,* **39**(5), 587–618.

Leurer, K.C. & Dvorkin, J., 2006. Viscoelasticity of precompacted unconsolidated sand with viscous cement, *Geophysics,* **71**(2), T31–T40.

Makarynska, D., Gurevich, B., Behura, J. & Batzle, M., 2010. Fluid substitution in rocks saturated with viscoelastic fluids, *Geophysics,* **75**(2), E115–E122.

Mallet, C., Quintal, B., Caspari, E. & Holliger, K., 2017. Frequency-dependent attenuation in water-saturated cracked glass based on creep tests, *Geophysics,* **82**(3), MR89–MR96.

Mavko, G., 2013. Relaxation shift in rocks containing viscoelastic pore fluids, *Geophysics,* **78**(3), M19–M28.

Mavko, G., Mukerji, T. & Dvorkin, J., 2009. *The Rock Physics Handbook: Tools for Seismic Analysis of Porous Media,* Cambridge Univ. Press.
Mikhaltsevitch, V., Lebedev, M. & Gurevich, B., 2016. Validation of the laboratory measurements at seismic frequencies using the Kramers-Kronig relationship, *Geophys. Res. Lett.,* **43,** 4986–4991.
Mikhaltsevitch, V., Lebedev, M., Gurevich, B., Sun, Y. & Glubokovskikh, S., 2019. A seismic-frequency laboratory study of solid substitution in Bentheim sandstone, *J. geophys. Res.,* **124,** 5492–5499.
Mori, T. & Tanaks, K., 1973. Average stress in matrix and average elastic energy of materials with misfitting inclusions, *Acta Metall.,* **21**(5), 571–574.
Nur, A., Mavko, G., Dvorkin, J. & Gal, D., 1998. Critical porosity: a key to relating physical properties to porosity in rocks, *Leading Edge,* **17**(3), 357–362.
Pimienta, L., Borgomano, J., Fortin, J. & Guéguen, Y., 2017. Elastic dispersion and attenuation in fully saturated sandstones: role of mineral content, porosity, and pressures, *J. geophys. Res.,* **122,** 9950–9965.
Quintal, B., Caspari, E., Holliger, K. & Steeb, H., 2019. Numerically quantifying energy loss caused by squirt flow, *Geophys. Prospect.,* **67,** 2196–2212.
Riviere, J. *et al.* 2016. Frequency, pressure, and strain dependence of nonlinear elasticity in Berea Sandstone, *Geophys. Res. Lett.,* **43,** 3226–3236.
Rubino, J.G. & Holliger, K., 2012. Seismic attenuation and velocity dispersion in heterogeneous partially saturated porous rocks, *Geophys. J. Int.,* **188**(3), 1088–1102.
Saxena, N. & Mavko, G., 2014. Exact equations for fluid and solid substitution, *Geophysics,* **79**(3), L21–L32.
Saxena, N. & Mavko, G., 2015. Effects of fluid-shear resistance and squirt flow on velocity dispersion in rocks, *Geophysics,* **80**(2), D99–D110.
Shapiro, S.A., 2003. Elastic piezosensitivity of porous and fractured rocks, *Geophysics,* **68,** 428–486.
Solazzi, S.G., Quintal, B. & Holliger, K., 2021. Squirt flow in porous media saturated by Maxwell-type non-Newtonian fluids, *Phys. Rev. E,* **103,** doi:10.1103/PhysRevE.103.023101.
Spencer, J.W., 2013. Viscoelasticity of Ells River bitumen sand and 4D monitoring of thermal enhanced oil recovery processes, *Geophysics,* **78**(6), D419–D428.
Subramaniyan, S., Quintal, B., Madonna, C. & Saenger, E., 2015. Laboratory-based seismic attenuation in Fontainebleau sandstone: evidence of squirt flow, *J. geophys. Res.,* **120,** 7526–7535.
Sun, C., Tang, G.Y., Fortin, J., Borgomano, J. & Wang, S.X., 2020. Dispersion and attenuation of elastic wave velocities: impact of microstructure heterogeneities and local measurements, *J. geophys. Res.,* **125,** e2020JB020132.
Sun, Y.Y. & Gurevich, B., 2020. Modeling the effect of pressure on the moduli dispersion in fluid-saturated rocks, *J. geophys. Res.,* **125**(8), e2019JB019297.
Sun, Y.Y., Gurevich, B., Glubokovskikh, S., Lebedev, M., Squeich, A., Arns, C. & Guo, J.X., 2019a. A solid/fluid substitution scheme constrained by pore-scale numerical simulations, *Geophys. J. Int.,* **220**(3), 1804–1812.
Sun, Y.Y., Gurevich, B., Lebedev, M., Glubokovskikh, S., Mikhaltsevitch, Y. & Guo, J.X., 2019b. A triple porosity scheme for fluid/solid substitution: theory and experiment, *Geophys. Prospect.,* **67,** 888–899.
Tsai, H.-C. & Lee, C.-C., 1998. Compressive stiffness of elastic layers bonded between rigid plates, *Int. J. Solids Struct.,* **70,** 381–389.
Vanorio, T., Nur, A. & Ebert, T., 2011. Rock physics analysis and time-lapse rock imaging of geochemical effects due to the injection of $CO_2$ into reservoir rocks, *Geophysics,* **76**(5), O23–O33.
Walsh, J.B, 1969. New analysis of attenuation in partially melted rocks, *J. geophys. Res.,* **74,** 4333.
Wolf, K., Vanorio, T. & Mavko, G., 2008. Measuring and monitoring heavy-oil reservoir properties, *Leading Edge,* **27,** 1138–1147.
Yin, H.J., Borgomano, J., Wang, S.X., Tiennot, M., Fortin, J. & Guéguen, Y., 2019. Fluid substitution and shear weakending in clay-bearing sandstone at seismic frequencies, *J. geophys. Res.,* **124,** 1254–1272.
Yin, H.J., Zhao, J.G., Tang, G.Y., Zhao, L.M., Ma, X.Y. & Wang, S.X., 2017. Pressure and fluid effects on frequency-dependent elastic moduli in fully saturated tight sandstone, *J. geophys. Res.,* **122,** 2017JB014244.
Yuan, H., Han, D.-H. & Zhang, W., 2016. Heavy oil sands measurement and rock-physics modeling, *Geophysics,* **81**(1), D57–D70.
Yuan, H., Han, D.-H. & Zhang, W., 2017. Seismic characterization of heavy oil reservoir during thermal production: a case study, *Geophysics,* **82**(1), B13–B27.
Zhang, M.F., He, Y.X., Wang, S.X., Tang, G.Y. & Sun, C., 2023. A benchmark study for quasi-static numerical upscaling of seismic wave attenuation and dispersion in fractured poroelastic rocks, *Comput. Geosci.,* **180,** 10549.
Zhao, L.X., Yuan, H.M., Yang, J.K., Han, D.H., Geng, J.H., Zhou, R., Li, H. & Yao, Q.L., 2017. Mobility effect on poroelastic seismic signatures in partially saturated rocks with applications in time-lapse monitoring of a heavy oil reservoir, *J. geophys. Res.,* **122,** 8872–8891.

## APPENDIX A: WORKFLOW FOR PORE MICROSTRUCTURE DISTRIBUTION CHARACTERIZATION

Rather than reproduce the detailed derivations (see de Paula *et al.* 2012; Glubokovskikh *et al.* 2016; Sun *et al.* 2019a, 2019b for more details), here we outline the main procedures of a plausible approach used to the dry ultrasonic velocities measurements for estimations of all key parameters in eqs (6)–(14) for fluid and solid substitution under the assumption that dry rock elastic properties (moduli and velocities) are independent of frequencies (non-dispersive). There is a comprehensive description give by He *et al.* (2024a) about calculation of pressure-dependent aspect ratio distribution and compliant porosities.

(1) Estimation of parameters ($\phi_c(P)$, $\alpha_c(P)$) characterizing the compliant pore microstructure as follows:

**Step 1** The distribution of total crack density $\Gamma$(P) at each pressure is obtained using

$$\Gamma\,(\mathrm{P}) = \Gamma_0 e^{-P/(PL)}, \tag{A1}$$

where $\Gamma_0$ is the initial crack density at zero pressure, and $PL$ refers to the compaction coefficient.

**Step 2** From the stress dependence of dry ultrasonic elastic properties ($K_{\mathrm{dry}}$, $G_{\mathrm{dry}}$), the broad distributions of crack aspect ratios $\alpha_c^i$ at each pressure can be directly extracted using (see David & Zimmerman 2012; Duan *et al.* 2018)

$$\alpha_c^i\,(P) = \alpha_{c0}^i - \int_0^P \frac{4\left(1-\upsilon_b^2\right)}{3K_{\mathrm{sp}}\,(1-2\upsilon_b)}\mathrm{d}P, \tag{A2}$$

where $K_{\mathrm{sp}}$ represents bulk modulus of an isotropic background containing evenly distributed stiff pores and, $\upsilon_b$ refers to Poisson's ratio for the rock frame. The aspect ratio of the $i$th unstressed compliant pore $\alpha_{c0}^i$ can be expressed using

$$\alpha_c^i = \frac{3}{4}\int_{\Gamma_0}^{\Gamma(\alpha)} \frac{[1/K_d\,(\Gamma_P) - 1/K_h]}{\Gamma_P}\frac{\mathrm{d}P}{\mathrm{d}\Gamma_P}\mathrm{d}P, \tag{A3}$$

where $K_d(\Gamma(P_i))$ is the bulk modulus at varying pressures, and $\Gamma(\alpha)$ denotes the total crack density at aspect ratio larger than $\alpha_0^i$.

**Step 3** The crack porosity distribution against the compliant aspect ratio at each pressure can be obtained using

$$\phi_c^i\,(\alpha_c) = \frac{4}{3}\pi\alpha_c^i\,(P)\,\Gamma\,(\alpha_c)\,, \tag{A4}$$

where $\Gamma(\alpha_c)$ is the cumulative crack density versus aspect ratio $\alpha_c$ of compliant pores for each pressure $P_i$ (see Fig. 10d) which can

be directly derived from the measured elastic velocities based on a least-squares fitting method.

(1) Estimation of parameters for intermediate pores ($\phi_{\rm m}(P)$, $\alpha_m$) using pressure dependence of dry elastic properties as follows:

**Step 1** When the dry rock elastic properties at relatively high pressures are available, the intermediate porosity $\phi_{\rm m}(P)$ can be obtained using the least-fitting of the stress-dependent dry rock moduli through the following relations:

$$K_{\rm cp}(P) = K_{\rm ep}\left[1 - \theta_m \phi_m(P)\right], \tag{A5}$$

$$G_{\rm cp}(P) = \mu_{\rm ep}\left[1 - \theta_m \phi_m(P)\right], \tag{A6}$$

where $\theta_m$ is pressure sensitivity coefficient for intermediate pores. There is a detailed description in He *et al.* (2022) about estimation of intermediate porosity using pressure dependence of dry elastic moduli.

**Step 2** Similar to compliant pores, the characteristic aspect ratio $\alpha_{\rm m}$ of the intermediate pores can be extracted by the expression for bulk modulus of an elastic medium with a dilute concentration of ellipsoidal cavities (e.g. Kuster & Toksöz 1974; de Paula *et al.* 2012)

$$\theta_m = \frac{K_{\rm ep}\left(3K_{\rm ep} + 4G_{\rm ep}\right)}{\pi\alpha_m G_{\rm ep}\left(3K_{\rm ep} + G_{\rm ep}\right)}. \tag{A7}$$

Moreover, the dry compressibility, $1/K_{\rm ep}$, can be calculated with effective medium theory based on the coherent potential approximation for the spherical pores. See Appendix C for detailed descriptions of the dependence of bulk and shear moduli, $K_{\rm ep}$ and $G_{\rm ep}$, of the dry background on rock porosity.

(1) Once the dry rock elastic moduli, the intermediate and compliant porosities and their associated aspect ratios are extracted, dynamic pressure relaxations induced rock elastic moduli can be calculated through eqs (6)–(9) or eqs (11) and (12) for the restructured rock matrix, in which both intermediate and compliant pores are fully saturated by solid or liquid substances while all equant pores are empty.

(2) Finally, we estimate the pressure- and frequency-dependent bulk and shear moduli in the fully saturated rock through the Gassmann eqs (12) and (13) for fluid or inviscid-liquid pore infill, or eqs (B1) and (B2) and the eqs (B3) and (B4) for solid or high-viscosity pore infill, accounting for the effects of combined squirt flows between the stiff and compliant pores and between the equant and intermediate pores. The theoretical predictions of elastic moduli in a saturated rock are then compared against the experimental measurements in the low seismic and high ultrasonic frequencies.

## APPENDIX B: EQUATIONS FOR FLUID AND SOLID INFILL SUBSTITUTION BASED ON CS AND SM MODELS IN AN ISOTROPIC HOMOGENEOUS ROCK

For an isotropic homogeneous bulk rock frame filled with a solid infill, the corresponding effective elastic properties, $K_{\rm CS}^{\rm solid}$ and $G_{\rm CS}^{\rm solid}$ (Ciz & Shapiro 2007) and $K_{\rm SM}^{\rm solid}$ and $G_{\rm SM}^{\rm solid}$ (Saxena & Mavko 2015), were calculated using the formula

$$K_{\rm CS}^{\rm solid} = \left[\frac{1}{K_{mf}} - \frac{\left(K_{mf}^{-1} - K_g^{-1}\right)^2}{\phi_s\left(K_f^{-1} - K_g^{-1}\right) + \left(K_{mf}^{-1} - K_g^{-1}\right)}\right]^{-1}, \tag{B1}$$

$$G_{\rm CS}^{\rm solid} = \left[\frac{1}{G_{mf}} - \frac{\left(G_{mf}^{-1} - G_g^{-1}\right)^2}{\phi_s\left(G_f^{-1} - G_g^{-1}\right) + \left(G_{mf}^{-1} - G_g^{-1}\right)}\right]^{-1}, \tag{B2}$$

and

$$K_{\rm SM}^{\rm solid} = K_d + \frac{\left(1 - \frac{K_d}{K_g}\right)^2}{\frac{\phi_s}{K_f} + \frac{1-\phi_s}{K_g} - \frac{K_d}{K_g^2}}, \tag{B3}$$

$$G_{\rm SM}^{\rm solid} = G_d + \frac{\left(1 - \frac{G_d}{G_g}\right)^2}{\frac{\phi_s}{G_f} + \frac{1-\phi_s}{G_g} - \frac{G_d}{G_g^2}}, \tag{B4}$$

where $G_{\rm g}$ is shear modulus of the grain mineral and,

$$K_d = \frac{(1-\phi_s)\left(\frac{1}{K_{\rm g}} - \frac{1}{K_{\rm mf}}\right) + \frac{3\phi_s}{4}\left(\frac{1}{G_{\rm g}} - \frac{1}{G_{\rm f}}\right)}{\frac{1}{K_g}\left(\frac{1}{K_{\rm g}} - \frac{1}{K_{\rm mf}}\right) + \frac{3\phi_s}{4}\left(\frac{1}{K_{\rm g}G_{\rm g}} - \frac{1}{K_{\rm mf}G_f}\right)}, \tag{B5}$$

$$G_d = \frac{(1-\phi_s)\left(\frac{1}{G_{\rm g}} - \frac{1}{G_{\rm mf}}\right) + \frac{3\phi_s}{4}\left(\frac{1}{E_g} - \frac{1}{E_f}\right)}{\frac{1}{G_{\rm g}}\left(\frac{1}{G_{\rm g}} - \frac{1}{G_{\rm mf}}\right) + \frac{3\phi_s}{4}\left(\frac{1}{G_{\rm g}E_{\rm g}} - \frac{1}{G_{\rm mf}E_{\rm f}}\right)}, \tag{B6}$$

$$E = \frac{\mu}{8}\frac{9K + 8\mu}{K + 2\mu}. \tag{B7}$$

## APPENDIX C: EXPRESSIONS OF BULK AND SHEAR MODULI OF DRY ROCK BACKGROUND

For the dry rock of a porous elastic solid, its bulk modulus can be represented as

$$K_{\rm dry} = K_0(1 - \beta), \tag{C1}$$

where $K_{\rm dry}$ and $K_0$ are the bulk moduli of the dry rock and solid mineral, respectively, and $\beta$ is the Biot's coefficient.

Krief *et al.* (1990) introduced a formula for $\beta$ versus $\phi$ empirically as follows:

$$1 - \beta = (1 - \phi)^{m(\phi)}, \tag{C2}$$

where $m(\phi) = 3/(1-\phi)$. For a sandstone mainly consisted of a single grain material (e.g. quartz), Poisson's ratio of the dry rock is often approximately equal to the mineral's Poisson's ratio, or $\mu_{\rm dry}/K_{\rm dry} = \mu_0/K_0$. Thus, the dependence of bulk and shear moduli ($K_{\rm ep}$, $G_{\rm ep}$) of the dry rock skeleton on porosity can be represented through the following empirical relation (see Krief *et al.* 1990)

$$\frac{K_{\rm sp}}{K_{\rm ep}} = \frac{G_{\rm sp}}{G_{\rm ep}} = (1 - \phi)^{3/(1-\phi)}, \tag{C3}$$

where $G_{\rm sp}$ denotes dry frame shear modulus of a hypothetical rock in which all soft pores are closed and the stiff porosity is equal to the magnitude at the unstressed condition. Please note that the linear forms of $K_{\rm sp}$ and $G_{\rm sp}$ predicted from the critical porosity model by Nur *et al.* (1998) are essentially the same as the formula in Krief *et al.* (1990) within the range of critical porosity.

## APPENDIX D: DESCRIPTIONS OF THE DIFFERENTIAL MORI-TANAKA MODEL

Our newly presented differential Mori-Tanaka model (DMT), which follows the idea of differential effective medium theory, considers a rock containing all kinds of pores with various geometries and is superior to the differential effective medium (DEM) theory and

Mori-Tanaka (MT) theory. The saturated mean moduli of equivalent rock can be described as follows:

$$K^*_{n+1} = K_n \left[ 1 + \sum_{i=1}^{N} \frac{\frac{\varphi_i}{1-\varphi_i} P^{\mathrm{mi}} \left(1 - \frac{K_i}{K_n}\right)}{1 - \frac{\varphi_i}{1-\varphi_i} P^{mi} \frac{K_i}{K_n}} \right]^{-1}, \tag{D1}$$

$$G^*_{n+1} = G_n \left[ 1 + \sum_{i=1}^{N} \frac{\frac{\varphi_i}{1-\varphi_i} Q^{\mathrm{mi}} \left(1 - \frac{G_i}{G_n}\right)}{1 - \frac{\varphi_i}{1-\varphi_i} Q^{\mathrm{mi}} \frac{G_i}{G_n}} \right]^{-1}, \tag{D2}$$

where $\varphi_i$ represents volume concentration for the $i$th inclusion in the summation over different pore types. $K_n$ and $G_n$ represent the bulk modulus and shear modulus of the rock matrix and, $K_i$ and $G_i$ denote the elastic moduli for the $i$th inclusion out of $N$. The terms $P^{\mathrm{mi}}$ and $Q^{\mathrm{mi}}$ are pore geometric factors that describe the effects of the $i$th inclusion with specific material and arbitrary aspect ratio in the background matrix $m$. The expressions of coefficients $P$ and $Q$ for four special pore geometries are presented in Table D1. Here, we used the DMT scheme to compute the dry bulk modulus as well as its high-pressure value to obtain the modified frame bulk modulus. Subsequently, using the equations of the three porosity structure model, we obtain the effective dynamic bulk modulus and shear modulus versus frequency and pressure for a saturated rock.

Here, $\gamma = \mu \frac{3K+\mu}{3K+7\mu}$, $\beta = \mu \frac{3K+\mu}{3K+4\mu}$, $\xi = \frac{K}{6} \frac{9K+8\mu}{K+2\mu}$, $\alpha$ represents aspect ratio of cracks, and a disk is a crack with zero thickness.

**Table D1.** Coefficients $P$ and $Q$ for four special pore geometries. Please note the subscripts $i$ and $m$ denotes the inclusion materials and background matrix (see Berryman 1995; Mavko *et al.* 2009).

| Pore shape | $P^{\mathrm{mi}}$ | $Q^{\mathrm{mi}}$ |
|---|---|---|
| Needles | $\frac{K_m+\mu_m+\frac{1}{3}\mu_i}{K_i+\mu_m+\frac{1}{3}\mu_i}$ | $\frac{1}{5}\left(\frac{4\mu_m}{\mu_m+\mu_i} + 2\frac{\mu_m+\gamma_m}{\mu_i+\gamma_m} + \frac{K_i+\frac{4}{3}\mu_m}{K_i+\mu_m+\frac{1}{3}\mu_i}\right)$ |
| Disks | $\frac{K_m+\frac{4}{3}\mu_i}{K_i+\frac{4}{3}\mu_i}$ | $\frac{\mu_m+\xi_i}{\mu_i+\xi_i}$ |
| Spheres | $\frac{K_m+\frac{4}{3}\mu_m}{K_i+\frac{4}{3}\mu_m}$ | $\frac{\mu_m+\frac{4}{3}\xi_m}{\mu_i+\frac{4}{3}\xi_m}$ |
| Penny cracks | $\frac{K_m+\frac{4}{3}\mu_i}{K_i+\frac{4}{3}\mu_i+\pi\alpha\beta_m}$ | $\frac{1}{5}\left(1 + \frac{8\mu_m}{8\mu_i+\pi\alpha(\mu_m+2\beta_m)} + 2\frac{K_i+\frac{2}{3}(\mu_i+\mu_m)}{K_i+\frac{4}{3}\mu_i+\pi\alpha\beta_m}\right)$ |